Deutsches Zentrum
für Luft- und Raumfahrt
German Aerospace Center

Ludwig-Maximilians-University of Munich
Department of Physics
Meteorological Institute Munich

LIDAR measurements: Determination of the aerosol extinction coefficient and comparison of incomplete overlap correction methods

Master Thesis

by

Juliane Ludwig

Ludwig-Maximilians-Universität München
Fakultät für Physik
Meteorologisches Institut

Deutsches Zentrum für Luft- und Raumfahrt
Institut für Solarforschung

LIDAR Messungen: Bestimmung des Extinktionskoeffizienten und Vergleich von Korrekturmethoden für den unvollständigen Überlapp

Eine Arbeit zur Erlangung des

akademischen Grades

Master of Science

vorgelegt von

Juliane Ludwig

12. Dezember 2014

Gutachter: Prof. Dr. Bernhard Mayer
Meteorologisches Institut München

Betreuerin: Natalie Hanrieder
DLR, Almería, Spanien

Abstract

The energy demand that accompanies the economic stability of the industrialized countries is steadily growing. As the stock of fossil fuels becomes extinct, the need of renewable energy resources emerges. The Concentrated Solar Power technology offers a climate-friendly alternative for the production of electricity in the renewable energy market. A key factor of the efficiency of a CSP plant is the extinction of the direct normal irradiance, due to scattering and absorption of light by molecules and particles. In this thesis elastic LIDAR measurements, corresponding to 33 h, have been performed at the Plataforma Solar de Almería and analyzed, using reference data of in-situ sun photometer and ceilometer measurements. With the application of the Klett-Fernald method the aerosol extinction coefficient and the aerosol optical depth (AOD) were determined for the 355 nm and 532 nm lidar wavelengths and analogous for the 1064 nm ceilometer wavelength. Sensitivity studies show that the choice of the reference height, the lidar ratio and the application of the background correction are of major importance for the Klett-Fernald method.

Furthermore, the AOD data sets of the LIDAR system, the sun photometer and the ceilometer were intercompared. The deviation between the LIDAR and sun photometer AODs indicates that the LIDAR system suffers from the overlap problem due to a lack of coincidence between the laser's and the receiver's fields of view at altitudes below 120 m. A comparison of ceilometer and LIDAR data reveals that the aerosol extinction coefficient and the according AOD determined with the ceilometer are smaller than the results obtained with the LIDAR. This was thought to be primarily due to the difference in operating wavelengths of both instruments. Therefore, a comparison of ceilometer data to sun photometer data was accomplished. To retrieve the AODs at the specific wavelength of 1064 nm, the Ångström approach has been applied to the sun photometer data. The AODs obtained with the ceilometer are also smaller than for sun photometer measurements leading to the assumption that a calibration of the ceilometer system is needed.

To correct the loss of signal of the LIDAR system in the incomplete overlap region, three different correction functions have been applied to the lidar backscatter signal. The aerosol density in the lower troposphere is expected to be higher than for greater altitudes, due to stirred-up dust and urban pollution. A correction function, therefore, must cause an amplification of the raw lidar backscatter signal in the lowest 120 m. The analytical correction function by Stelmaszczyk et al. (2010) is evolved from geometric considerations and has a small impact on the AOD for the 355 nm wavelength and no impact for the 532 nm wavelength and is therefore not suitable for the correction of the lidar signal. The correction function proposed by Biavati et al. (2011), derived from on an iterative approach from angular measurements, results in an "over-correction" of the signal. The third correction method proposed by Guerrero-Rascado et al. (2010) is iteratively achieved by comparison to the ceilometer attenuation coefficient at low altitudes and suits for the correction of the lidar signal.

Finally, the lidar extinction coefficient at 90 m altitude, obtained firstly from tilted measurements and secondly from the overlap corrected vertical signal, is compared to a Vaisala FS11 scattermeter data set. The results prove that the correction function by Guerrero-Rascado et al. (2010) is best suited for the LIDAR system.

Contents

Nomenclature

$\alpha(r, \lambda)$	Extinction Coefficient
$\alpha_{aer}(r, \lambda$	Aerosol Extinction Coefficient
$\alpha_{mol}(r, \lambda$	Molecular Extinction Coefficient
$\beta(r, \lambda)$	Backscatter Coefficient
$\beta_{aer}(r, \lambda$	Aerosol Backscatter Coefficient
$\beta_{att}(r, \lambda$	Attenuated Backscatter Coefficient
$\beta_{mol}(r, \lambda$	Molecular Backscatter Coefficient
δ	Depolarization Factor
ϵ	System Efficiency
ι	Particle Radius
λ_0	Limiting Wavelength (500 nm)
λ_1	Reference Wavelength for B (1000 nm)
μ	Laser Beam Divergence
$\nu(r)$	Geometrical Displacement
ω	Elevation Angle
Φ	Telescope's Field of View
τ	Time of Flight
τ_t	LIDAR System's Dead Time
θ	Laser Inclination Angle
A	Area of the Primary Receiver Optics
A_1	Ångström Wavelength Exponent for $\lambda < \lambda_0$
A_2	Ångström Wavelength Exponent for $\lambda > \lambda_0$
B_1	Ångström Turbidity Coefficient for $\lambda < \lambda_0$
B_2	Ångström Turbidity Coefficient for $\lambda > \lambda_0$
c	Velocity of Light
D	Primary Mirror Diameter
d_0	Distance between Laser Beam Exit and Receiver
$e(r)$	Area of Illumination inside the Telescope's FOV
E_{det}	Energy Transferred to Photodetector
E_{scat}	Energy Reaching the Telescope's Primary Mirror
f	Focal length
$F(r)$	Overlap Area
g_0	Initial Beam Diameter
h	Scaling Height
LR	Aerosol Lidar Ratio
LR_{mol}	Molecular Lidar Ratio
M	Number of Aerosol Components
m_i	Refractive Index of Aerosol Components
N	Observed Count Rate
n_a	Refractive Index of Air
n_i	Lognormal Distribution of Aerosol Components
N_S	Number Density of Molecules

n_S	Refractive Index of Air at Standard Conditions
N_{S0}	Number Density of Molecules in Air at Standard Conditions
$O(r)$	Correction function
$P(r, \lambda)$	Measured Backscatter Power
P_0	Laser Pulse Power
p_0	Pressure at Standard Conditions
p_g	Pressure at Ground Level
$Q_{Back}(\iota, m_i, \lambda)$	Backscatter Efficiency
$Q_{Ext,i}(\iota, m_i, \lambda)$	Extinction Efficiency
r	Range
$R_{min,Ceilo}$	Full-Overlap Distance Ceilometer
R_{min}	Full-Overlap Distance LIDAR
r_{ref}	Reference Height
S	True Count Rate
s	Aperture of Telescope
t	Time
T^2	Transmission Term
T_0	Temperature at Standard Conditions
T_g	Temperature at Ground Level
X_1	Signal from Vertical Measurement
X_2	Signal from Angular Measurement

List of Abbreviations

AERONET	Aerosol Robotic Network
AOD	Aerosol Optical Depth
AOT	Aerosol Optical Thickness
APD	Avalanche Photodiode
ASCII	American Standard Code for Information Interchange
CSP	Concentrated Solar Power
DAC	Digital to Analog Converter
DIAL	Differential Absorption LIDAR
DNI	Direct Normal Irradiance
FOV	Field of View
LIDAR	Light Detection and Ranging
MD	Mean Difference
PBL	Planetary Boundary Layer
PM	Photomultiplier
PMT	Photomultiplier Tube
PSA	Plataforma Solar de Almería
RCS	Range-Corrected Signal
RMS	Root Mean Square
SNR	Signal-to-Noise Ratio
STD	Standard Deviation
UV	Ultraviolett
VIS	Visible

1 Introduction

The energy needs of the world will continue to grow rapidly in the upcoming years. While the energy consumption of industrialized countries is growing more slowly, there are many emerging countries with high economic growth resulting in a large backlog. In addition, the world's population will increase rapidly in the upcoming decades. This increases the problems of today's energy supply and the consequences of global warming. As the stocks of fossil fuels will run out, the demand of renewable energy will prevail and technologies with great development potential and less impact on the environment are of major interest [Quaschning, 2012]. Such a sustainable energy source is found in solar radiation.

Concentrated solar power (CSP) is used to produce electricity. The CSP technology includes mirror systems, that focus the sun's direct normal irradiance (DNI) onto a receiver.

In the case of a solar tower power plant the solar radiation is reflected by a mirror system (heliostat field) and consequently the light path is extended by the distance between the respective heliostats and the receiver at the tower [Hanrieder et al., 2012]. This distance is comparably large to other CSP technologies, e.g dish stirling systems or parabolic through systems. In the lowest 100 m of the troposphere the attenuation of light is particularly high, leading to a great impact on the efficiency of a solar power tower plant [Quaschning, 2012]. For that reason, the attenuation of solar light and gaining knowledge of pollutants that attenuate the direct normal irradiance from the sun is the subject of many investigatory projects that deal with solar energy and aim to improve the efficiency of solar power plants [Guerrero-Rascado et al., 2008].

So far, the plant optimization tools are based on standard atmospheric conditions for determination of light attenuation, neglecting special local atmospheric conditions, e.g. low-level haze or situations present close to aerosol sources [Hanrieder et al., 2012]. In most cases only one hazy and one clear situation is optional while performing power plant performance simulations. One improved model (Pitman Vant-Hull) was developed which also allows site-dependent input of several meteorological parameters [Pitman and Vant-Hull, 1982]. But still it is assumed that the aerosol density decreases exponentially with the site altitude and the height over ground [Pitman and Vant-Hull, 1982]. This model can be improved when local parameters, like the tower height, absolute air humidity and the site altitude are considered [Hanrieder et al., 2012]. Therefore, detailed investigations regarding the attenuation of solar irradiance in the lower troposphere are carried out at the Plataforma Solar de Almería (PSA). The PSA is located in the semi-desert of Tabernas, in 30 km distance to the Mediterranean Sea in Southern Spain. The location of the research facility is specifically chosen to observe similar meteorological conditions as encountered for a probable position of a CSP power plant.

A special opportunity for gaining information about local atmospheric conditions offer LIDAR measurements.

LIDAR systems have widely been used for remote sensing of the atmosphere [Stoyanov et al., 2012]. LIDAR stands for Light Detection and Ranging and is an optical analogue to the RADAR technique. Light, in the form of laser pulses, is emitted into the atmosphere, where it is scattered or reflected by particles or molecules. Its high resolution, sensitivity and accuracy in sensing atmospheric particles makes the LIDAR

method advantageous in comparison to other remote sensing techniques, e.g. radars [Stoyanov et al., 2012].

With an elastic LIDAR instrument it is possible to analyze the attenuation of solar irradiance in the lower troposphere with a high temporal and spatial resolution. From lidar profiles, important meteorological parameters such as the backscatter coefficient and the extinction coefficient, as a measure of attenuation of direct irradiance of the sun, can be determined. Also, the aerosol optical depth or the Ångstrom exponent can be derived, making it possible to observe phenomena like volcanic ash and Saharan dust with temporal evolution [Wiegner et al., 2012, Groß et al., 2011]. A significant limitation of the LIDAR technology is the strength of the laser signal and the general construction of a biaxial LIDAR system, where the vertical axes of the laser and the receiver are not aligned.

For the LIDAR system installed at the PSA, the signals below 120 m are incomplete because of the overlap effect. This effect is due to the lack of coincidence between the field of view (FOV) of the laser and the receiver, causing a loss of signal in the region of incomplete overlap. As for CSP power plants the attenuation of solar radiation in the atmospheric layer close to the ground is of special interest, the signal in this region needs to be corrected using a correction function.

The aim of this thesis is to determine the extinction coefficient profiles which can be derived from the data acquired by the LIDAR system installed at the Plataforma Solar de Almería. A comparison to available reference data from the sun photometer and the ceilometer is made. Furthermore, concrete correction functions for the region of incomplete overlap are implemented, intercompared and evaluated.

In the following section, the scientific background and theory of LIDAR is explained. Special focus was laid on the assumptions that have to be applied for the determination of the aerosol extinction coefficient from LIDAR measurements and the approaches to overcome the problem of incomplete overlap. In section 3, the underlying methods for LIDAR, ceilometer and sun photometer measurements are explained, in terms of the measurement principle, data collection and data processing. Within section 4, the results are shown, presenting inter alia data acquired for several months of measurement. The aerosol extinction coefficient is calculated using the data from LIDAR measurements and the sensitivity of the determination method is discussed. Also, the results for the different sensors are intercompared and discussed. The different overlap correction functions are displayed and their impact on the calculation method for the aerosol extinction coefficient is discussed. Further, a comparison to a Vaisala FS11 scattermeter data set is shown. The scattermeter measures the meteorological optical range and therefore the extinction coefficient from scattering of light in a small volume of air. In section 5, a conclusion is drawn from the accomplished results and an outlook is given.

2 Scientific Background and Theory

2.1 Atmospheric Extinction

Atmospheric extinction is a measure of the attenuation of solar radiation per length, due to absorption and scattering. There are two types of scattering that need to be distinguished: Rayleigh scattering and Mie scattering. Rayleigh scattering is the elastic scattering of light by molecules of small size in comparison to the wavelength [Zdunkowski et al., 2007]. Consequently, the Rayleigh atmosphere is then defined as region where aerosols are nearly non-existent and light scatters only on atmospheric molecules, like nitrogen, oxygen or argon [Sneep and Ubachs, 2005, Fröhlich and Shaw, 1980]. The Rayleigh atmosphere is expected at altitudes above 4000 m, if no special weather conditions are present, e.g. saharan dust cloud [Guerrero-Rascado et al., 2008]. Scattering by spherical shaped atmospheric particles with diameter bigger than the scattered wavelength is described by Mie-theory [Zdunkowski et al., 2007]. Regarding atmospheric aerosols, there is a great variety that can be classified with respect to their source region, such as: marine, desert dust, urban haze, arctic haze, forest fire smoke and north/east asian aerosol [Müller et al., 2007]. A further distinction can be made with respect to the solubility of those aerosol types, i.e. water soluble or insoluble and to aerosol components, like soot, mineral or sea salt.

Besides the scattering by particles and molecules, another aspect causing the attenuation of sunlight in the atmosphere is absorption. Propagating photons can get absorbed by atoms or molecules changing the state of the absorbing system [Zdunkowski et al., 2007]. The main absorbers in the visible spectrum are ozone, water vapor and oxygen [Ackermann, 1998]. The absorbing properties of those gases are the basis of investigatory methods, like Differential Absorption LIDAR (DIAL). In contrast, taking elastic LIDAR measurements, the wavelength is chosen in a way that it will not get absorbed by one of the major gas contributions in air.

Another measure of the loss of solar radiation in the atmosphere is the aerosol optical depth (AOD), also called aerosol optical thickness (AOT). The aerosol optical depth as a measure of transparency is defined as the integral of the aerosol extinction coefficient from ground up to the reference height [Benito, 2001]:

$$AOD(r) = \int_0^{r_{ref}} \alpha_{aer}(r, \lambda) \mathrm{d}r'. \tag{1}$$

The AOD states how much direct sunlight is prevented from reaching the ground by aerosol particles. It is a dimensionless number that is related to the total amount of aerosol in the vertical column of atmosphere from ground to a defined height [Parsiani and Bonilla, 2008]. A value of 0.01 corresponds to an extremely clear atmosphere, a value of 0.4 would correspond to a hazy condition and a value of 1 describes cloudy conditions [AERONET, 2014].

2.2 LIDAR and its Applications

LIDAR measurements are temporal and spacial resolved measurements of backscattered photons. Light pulses are emitted into the atmosphere, where they are scattered in different heights by particles or molecules. Backscattered photons are detected by a

telescope. The strength of the received backscatter signal depends on the attenuation, due to scattering and absorption processes of the light along its path.

From the backscatter signal, the backscatter and extinction coefficients can be derived together with the cloud base height. LIDAR measurements also enable the remote detection of environmentally important trace gases like ozone. LIDAR systems find application in a variety of research fields, like atmospheric science, astronomy, nuclear fusion and also geology, where they are used for surface mapping, forestry and shoreline morphology [Kovalev, 2004]. Economic applications are volcanic and fire alerting, military, aviation, robotics and transportation. As manifold as the applications, as diversive are the LIDAR systems.

There exist ground-based, air-borne and space-borne LIDAR variants, each can also differ in their schematics, regimes of operation, monitored parameters and construction [Kovalev, 2004]. Frequently used for remote sensing of the atmosphere are Raman LIDAR systems, that measure, besides the elastically backscattered light, signals caused by inelastic scattering. The change in energy of emitted and detected light yields information about the type of molecule. Another widespread type of LIDAR systems is the Differential Absorption LIDAR, which is used for the determination of particle concentrations. Two different wavelengths are emitted into the atmosphere, where one wavelength is chosen, such that it is absorbed by the substance, whereas the other is particularly not absorbed. A comparison of both signals allows to draw conclusions about the concentration of the substance. Generally, polarized wavelength measurements yield additional information about the size of particles.

Since the early 1960s LIDAR systems have successfully been used in remote sensing of the atmosphere. They have been applied in local and global-scale studies of atmospheric aerosols and climate-relevant gases such as ozone or vapor as well as for analyzing the properties of clouds and for dynamic processes within the planetary boundary layer [Stelmaszczyk et al., 2005, Goyer and Watson, 1963].

From unpolarized elastic LIDAR measurements it is not possible to get definite information about the type, size or concentration of particles. Other parameters like the extinction or attenuated backscatter coefficients have to be derived from the raw backscatter signal using mathematical approaches, where besides the limited number of laser wavelengths, the number and accuracy of assumptions influence the results, as described in sections 2.4 and 2.5. The LIDAR installed at the PSA is of the type elastic backscatter LIDAR, with two receiving channels in the UV and VIS optical range.

LIDAR is a remote sensing technology consisting of a transmitter, that illuminates a sample, a receiver, that collects the backscattered photons and an analyzing unit that monitors the signal. LIDAR systems are used inter alia to generate a 3-dimensional map of the lower atmosphere. For this purpose, a laser emits light pulses through emission optics that filter and focus the wanted wavelengths into the atmosphere, where it scatters by aerosols or particles. The backscattered radiation is detected by the attached receiving optics. The spectral analyzer filters the radiation for the wavelengths that correspond to elastic scattering events. Dichroic beam-splitters form the LIDAR spectral channels for initial wavelength separation of the backscattered laser radiation [Stoyanov et al., 2012]. Usually, narrow bandpass interference filters are installed to provide spectrally selected wavelengths and suppress the solar radiation background, especially in day-time measurements. A photodetector then detects the selected photo signal. By numerical analysis a monitoring and recording of the signal is accomplished

with the embedded data acquisition unit. Being a time-of-flight technique, the time delay between emission and return of the photons is measured, which provides information about the distance at which the photons were scattered, allowing a finely graduated spatial resolution of the detected signal. Also, a high temporal resolution along the line of the laser beam is given through multi-pulse measurements. The LIDAR method is the basis of ceilometer and LIDAR systems. The components of the LIDAR system at the PSA are described in detail in section 3.1.1.

2.3 LIDAR Equation

To retrieve vertical aerosol profiles, the data from the LIDAR's elastic channels are analyzed using the LIDAR equation. This equation expresses the relation between the range-resolved backscattered average power received by the photo detector and atmospheric and system parameters [Stoyanov et al., 2012]. The measured backscatter power $P(r, \lambda)$ detected at a time t is found to be:

$$P(r,\lambda) = P_0 \frac{c\tau}{2} A\epsilon \cdot \frac{O(r)}{r^2} \cdot \beta(r,\lambda) \cdot \exp\left(-2\int_0^r \alpha(r,\lambda)\mathrm{d}r\right), \tag{2}$$

where the first term, $P_0 \frac{c\tau}{2} A\epsilon$, on the right hand side is a system constant [Klett, 1981, Kovalev, 2004]. This constant explicitly consists of the laser pulse power P_0 with the unit $[W]$ and the geometric length from the laser to the scattering point from which the light reaches the photo receiver $c\tau$, where c is the velocity of light with the unit $\left[\frac{m}{s}\right]$ and τ is the time of flight with the unit $[s]$. $c\tau$ is divided by 2, because the LIDAR reports a two-way-attenuation. The term also includes the area of the primary receiver optics A in $[m^2]$ and the unknown system efficiency ϵ [Kovalev, 2004]. The system efficiency of the optics and electronics may vary between 0 and 1, where 1 would correspond to a system without energy losses. The second term $\frac{O(r)}{r^2}$ takes the distance-dependent geometry of the system into account. $O(r)$ denotes the unitless correction function that corrects the lack of coincidence of the laser beam and the receiver field of view for ranges below the complete overlap height, later described in section 2.6. r is the distance between the laser exit and the point of scattering in the atmosphere, commonly measured in $[m]$. Further, $\alpha(r, \lambda)$ and $\beta(r, \lambda)$ denote the height and wavelength dependent extinction and backscatter coefficients with units $\left[\frac{1}{m}\right]$ and $\left[\frac{1}{m \cdot sr}\right]$, respectively. The extinction coefficient describes how strongly light at a given wavelength is scattered and absorbed. The backscatter coefficient refers only to scattering events. Because the wavelength λ, given in $[m]$, is usually held constant during measurements, the wavelength dependency of the according parameters is no longer indicated. $\beta(r)$ forms together with pressure- and temperature profiles the transmission term $T^2(r)$. The transmission term refers to the transmission between the LIDAR system and the altitude and is indirectly stated in the LIDAR equation as $\alpha(r, \lambda)$ and $\beta(r, \lambda)$. The attenuated backscatter coefficient is then defined as:

$$\beta_{att}(r) = \beta(r) \cdot T^2(r), \tag{3}$$

which is a common expression for the attenuation of light for the range from the transmitter to the scattering sample and back to the receiver [Guerrero-Rascado et al.,

2010]. The LIDAR equation does not include terms that account for background correction and multiple scattering events. The background correction is discussed in section 2.5.3 and 4.1.3 and refers to a signal correction that accounts for the detected solar background radiation.

2.4 Methods to Solve the LIDAR Equation

The LIDAR equation requires independent information about at least three unknown physical parameters, such as the backscatter coefficient, the extinction coefficient and the systems efficiency. To gain information about the atmospheric extinction of light, the LIDAR equation needs to be inverted either for the backscatter coefficient or the extinction coefficient. But the quantitative retrieval of the backscatter and extinction coefficient is elusive and many different methods have been developed that aim to solve the LIDAR equation [Bissonnette et al., 2002].

In homogeneous atmospheres, the extinction coefficient can be determined by the inversion of lidar signals using the slope method based on angular measurements [Kunz and de Leeuw, 1993, Kovalev, 2004]. The simplifying hypothesis of a homogeneous atmosphere provides just two scalars, rather than two vectors, as the total extinction and backscatter estimates. Another approach is the Monte Carlo method, which relies on extensive analytic calculations [Bissonnette et al., 2002, Gutkowicz-Krusin, 1993].

Another method to extract the attenuation and backscatter coefficients from the return signal of a monostatic single-wavelength LIDAR system is the Klett method. It is valid for inhomogeneous atmospheres and does not need assumptions regarding a horizontal or vertical homogeneity of atmospheric stratification. According to Klett et al.(1981), this method assumes the validity of the power law between the backscatter and attenuation coefficient, see detailed in section 2.5 and equation 5. The firstly proposed solution, called *near-end solution*, for the LIDAR equation by Klett et al. (1981) assumed a reference distance r_0 for integration, see equation 10. This solution includes a mathematical instability in the calculations in the sense that small errors in the determination of the backscatter coefficient at the reference distance r_0 produce negative values for the backscatter coefficient over the sounded range [Stoyanov et al., 2012]. To solve this problem, Klett (1985) proposed an inverse integration method, starting from the far-end on the lidar sounding path, which is for historical reason called Klett-Fernald method or Klett-Fernald-Sasano method. The reference height r_{max} is chosen such that the aerosol backscatter coefficient is negligible compared to the molecular backscatter coefficient. In contrast to the earlier proposed solution, this method is claimed to be stable with respect to perturbations in the signal and the estimated boundary value [Klett, 1981]. Therefore in this thesis Klett's *far-end solution* is implemented and applied to the data acquired with the LIDAR system to calculate the backscatter and extinction coefficient.

Outside of the applicable options for an elastic LIDAR there exist also approaches that aim to eliminate the need of a boundary value in the far-end region, as in the high spectral resolution and Raman LIDAR methods [Shipley et al., 1983, Ansmann et al., 1990].

2.5 Derivation of the Extinction Coefficient Using the Klett-Fernald method

The Klett-Fernald method proposed by Klett et al. (1981) and Fernald et al. (1972) is an analytical inversion solution for the LIDAR equation [Klett, 1981, Fernald et al., 1972]. With this method the backscatter and extinction coefficients can be derived from the attenuation of the laser pulse energy starting at an estimated reference height r_{ref}. The main assumption is that the aerosol lidar ratio LR_{aer} is held constant, independent of time and range, causing high errors. In order to solve the LIDAR equation it is useful to split the backscatter and extinction coefficients, $\beta(r)$ and $\alpha(r)$, in molecular and aerosol terms, respectively and define the reference height. The reference height r_{ref} is the altitude at which only a Rayleigh atmosphere is assumed, meaning almost only scattering on molecules takes place above this height, as explained in subsection 2.1:

$$\begin{aligned} \alpha(r) &= \alpha_{mol}(r) + \alpha_{aer}(r) \\ \beta(r) &= \beta_{mol}(r) + \beta_{aer}(r). \end{aligned} \tag{4}$$

An approximate relation between $\beta(r)$ and $\alpha(r)$ is expressed by the empirical power law relationship [Klett, 1981]:

$$\beta(r) = const \cdot \alpha(r)^k, \tag{5}$$

where *const* stands for an empirical value dependent on the properties of the scatterer and the exponent k is range independent but a function of the laser wavelength and generally lies in the interval from $0.67 \leq k \leq 1.0$ [Curcio and Knestrick, 1958]. For analysis purposes, a convenient form for the received power is introduced, where RCS stands for the range-corrected signal:

$$P(r) = \ln\left(P(r) \cdot r^2\right) = \ln\left(RCS\right). \tag{6}$$

A range correction is needed because the raw backscatter signal is of an exponentially decreasing form, due to multi-scattering events in the atmosphere. In general holds: $RCS = P(r) \cdot r^2$. Using equation 4 and 6 and the known reference power $P(r_0)$ at the minimum range r_0 for the overlap of the receiver's and transmitter's fields of view, the LIDAR equation for $r \geq r_0$ can be written as:

$$P(r) - P(r_0) = \ln\left(\frac{\beta(r)}{\beta(r_0)}\right) - 2\int_{r_0}^{r} \alpha(r')\mathrm{d}r'. \tag{7}$$

Differentiation of both sides with respect to the range yields:

$$\frac{\mathrm{d}P(r)}{\mathrm{d}r} = \frac{1}{\beta(r)} \cdot \frac{\mathrm{d}\beta(r)}{\mathrm{d}r} - 2\alpha(r) \tag{8}$$

and with the substitution of equation 5 follows:

$$\frac{\mathrm{d}P(r)}{\mathrm{d}r} = \frac{k}{\alpha(r)} \cdot \frac{\mathrm{d}\alpha(r)}{\mathrm{d}r} - 2\alpha(r). \tag{9}$$

This nonlinear differential equation has the form of a Bernoulli or homogeneous Ricatti differential equation [Ince, 1956]. By using a linearization transformation ($n = 1/\alpha(r)$), the resulting solution of the differential equation is [Klett, 1981]:

$$\alpha(r) = \frac{\exp\left[\left(P(r) - P(r_0)\right)/k\right]}{\frac{1}{\alpha(r_{ref})} - \frac{2}{k}\int_{r_0}^{r} \exp\left[\left(P(r') - P(r_0)\right)/k\right] \mathrm{d}r}. \tag{10}$$

The structure of this formula is unstable, showing singularities regarding an imprecise determination of $\alpha(r_0)$. In 1985 Klett introduced a reference range r_{ref}, that generates a more stable solution for $r \leq r_{ref}$. The extinction coefficient $\alpha(r)$ is now determined as the ratio of two numbers, that progressively become larger:

$$\alpha(r) = \frac{\exp\left[\left(P - P(r_{ref})\right)/k\right]}{\frac{1}{\alpha(r_{ref})} + \frac{2}{k}\int_{r}^{r_{ref}} \exp\left[\left(P - P(r_{ref})\right)/k\right] \mathrm{d}r'}. \tag{11}$$

This solution is called *near-end solution* because, instead of integrating forward up to a *far-end range* r as in solution 11, it contains an inverse integration from a defined reference height r_{ref}. To transform the LIDAR equation into the desired form, equation 7 is reinserted and the particular or aerosol lidar ratio LR_{aer} is defined:

$$LR_{aer}(r) = \frac{\alpha_{aer}(r)}{\beta_{aer}(r)}, \tag{12}$$

with the unit $[sr]$. The aerosol lidar ratio LR_{aer} is the particle extinction-to-backscatter ratio that depends on range r, shape and chemical composition of the aerosol particles. For further considerations LR_{aer} is referred to as the lidar ratio LR. When deriving the extinction coefficient, the lidar ratio is usually considered to be height and time independent, $LR := const.$. The specification of the unknown lidar ratio constitutes a major source of error up to 100 % for the calculations of the backscatter and extinction coefficient. That means that a variation in the lidar ratio may change the extinction/backscatter coefficient by two orders of magnitude [Sasano et al., 1985, Ansmann et al., 1992].

It is assumed that the atmospheric absorption at the wavelength λ is negligible and the molecular extinction-to-backscatter ratio LR_{mol} is constant over a wide range of altitude r:

$$LR_{mol}(r) = \frac{\alpha_{mol}(r)}{\beta_{mol}(r)} = \frac{8\pi}{3}. \tag{13}$$

Rearranging equation 10 and inserting the above definitions 12 and 13 yields the desired form of the LIDAR equation for the total backscatter coefficient [Raymetrics, 2012]:

$$\beta(r) = \frac{RCS(r)\cdot\exp\left(2\cdot(LR-LR_{mol})\cdot\int_{r}^{r_{ref}}\beta_{mol}(r')\ \mathrm{d}r'\right)}{\frac{RCS\left(r_{ref}\right)}{C\cdot\beta_{mol}\left(r_{ref}\right)} + 2\cdot LR\cdot\int_{r}^{r_{ref}} RCS(r')\cdot\exp\left(2\cdot(LR-LR_{mol})\cdot\int_{r'}^{r_{ref}}\beta_{mol}(r'')\mathrm{d}r''\right)\mathrm{d}r'}. \tag{14}$$

With the knowledge of the backscatter coefficient $\beta(r)$, the aerosol extinction coefficient α_{aer} can be determined with:

$$\alpha_{aer}(r) = LR \cdot \left(\beta(r) - \beta_{mol}(r)\right). \tag{15}$$

Usually, at r_{ref} one assumes that the aerosol extinction coefficient $\beta_{aer}(r_{ref})$ equals zero, so that $C = 1$ and [Raymetrics, 2012]:

$$C = \frac{\beta_{aer}(r_{ref}) + \beta_{mol}(r_{ref})}{\beta_{mol}(r_{ref})}. \tag{16}$$

A range correction is applied because the backscatter signal behaves exponentially decaying in intensity due to the exponentially decreasing number density of particles with altitude. To retrieve the molecular backscatter coefficient $\beta_{mol}(r)$ from equation 13, the molecular extinction- or Rayleigh scattering coefficient has to be determined, which is given as:

$$\alpha_{mol}(r) = \frac{8\pi^3}{3 \cdot \lambda^4} \cdot \frac{1}{N_S(r)} \cdot \left[\frac{n_a^2 - 1}{n_a^2 + 1}\right]^2 \cdot \frac{6 + 3\delta}{6 - 7\delta} \cdot \frac{T_0}{p_0} \cdot \frac{p(r)}{T(r)}, \tag{17}$$

where N_S is the number density of molecules in $[m^{-3}]$), n_a is the dimensionless refractive index of air, δ is the depolarization factor, p and T are pressure and temperature with units $[hPa]$ and $[K]$, where the index 0 refers to standard conditions $T_0 = 288.15\,\mathrm{K}$ and $p_0 = 1013\,\mathrm{hPa}$, respectively [Fröhlich and Shaw, 1980]. The term $\frac{6+3\delta}{6-7\delta}$ was added to the Rayleigh formula by King (1923) and results in an invariance of the formula with respect to the details of molecular structure, as number and magnitude of dispersion charges, their position, and their orientation for anisotropic molecules [King, 1923]. In the atmosphere the refractive index n_a and the molecular number density N_S depend on pressure and temperature and hence on height. According to the Lorentz-Lorenz equation, the term $(n_a^2 - 1)/(n_a^2 + 1)$ is proportional to N_S, and therefore the following expression is commonly substituted in the Rayleigh formula of α_{mol}:

$$\frac{(n_a^2 - 1)^2}{N_S} = \frac{(n_S^2 - 1)^2}{N_{S0}} \cdot \frac{N_S}{N_{S0}}, \tag{18}$$

where n_S is the refractive index and N_{S0} is the number density of molecules of air at standard conditions, respectively [Kittel, 1976, Fröhlich and Shaw, 1980]. N_S can be calculated using:

$$N_S(r) = N_{S0} \cdot \frac{p_g}{T_g} \cdot \exp\left(-\frac{r}{h}\right), \tag{19}$$

with p_g and T_g as the pressure and temperature at ground level and h as the scaling height. Applying the substitution to equation 17 it yields:

$$\alpha_{mol}(r) = \frac{8\pi^3}{3} \cdot \frac{(n_S^2 - 1)^2}{\lambda^4 N_{S0}^2} \cdot \frac{6 + 3\delta}{6 - 7\delta} \cdot N_S(r) \cdot \frac{T_0}{p_0} \cdot \frac{p(r)}{T(r)} \tag{20}$$

for the molecular extinction coefficient.

2.5.1 Reference Height

The values for the reference height and the lidar ratio have to be chosen very carefully because both represent important factors with large impact on the results of the calculation for the backscatter and extinction coefficient. The reference height r_{ref} is normally chosen to be the altitude where a nearly aerosol-free zone in the upper free Troposphere begins. Scattering by molecules is the dominant process at this altitude. The predetermination of the reference height allows a differentiation between

the molecular and aerosol backscatter coefficients. The total molecular backscatter coefficient at a wavelength λ for the pressure p and temperature T and the number density N is found to be:

$$\beta_{mol}(r) = \frac{\pi^2 \left(n_S^2 - 1\right)^2}{\lambda^4 N_{S0}^2} \cdot \frac{6 + 3\delta}{6 - 7\delta} \cdot N_S(r) \cdot \frac{T_0}{p_0} \cdot \frac{p(r)}{T(r)}, \tag{21}$$

where δ is the depolarization factor, $p_0 = 101.325\,\text{kPa}$, $T_0 = 288.15\,\text{K}$ and $N_{S0} = 2.547 \cdot 10^{19}\,\text{cm}^{-3}$ are pressure, temperature and number density at standard atmospheric conditions, respectively [Kovalev, 2004]. According to [Mattis et al., 2008] the reference height is situated between 5 km and 7 km. The sensitivity of the determination of the extinction coefficient using the Klett-Fernald method with respect to the reference height r_{ref} is discussed later in section 4.1.1. The derived backscatter coefficient from the reference height is similar to the backscatter coefficient solely based on scattering by molecules. Knowledge of this parameter provides information about the adjustment of the LIDAR system and is therefore called Rayleigh calibration.

2.5.2 Lidar Ratio

Another value that needs to be chosen when calculating the backscatter and extinction coefficient and the resulting AOD with the Klett-Fernald method is the lidar ratio. The lidar ratio LR is defined as the ratio of particle extinction- and backscatter coefficient, i.e. on two optical parameters that depend on the wavelength of the incident light [Ackermann, 1998]. The lidar ratio varies for aerosol types and depends on the aerosol structure, size and composition. Another factor that influences the LR is the relative humidity, which increases often with altitude within the planetary boundary layer (PBL). Pressure- and temperature profiles include information about the relative humidity and are usually taken into account when an elastic lidar profile is acquired. For that reason, different lidar ratios have to be determined according to different climatic environments [Müller et al., 2007]. From Raman LIDAR, sun photometer and optical counter measurements mean lidar ratios have been found to lie between 19.5 sr and 70 sr for varying wavelengths between 355 nm and 1064 nm [Takamuka et al., 1994, Waggoner et al., 1972], estimated with respect to the measurement location and atmospheric conditions. Using Mie theory, the extinction efficiency $Q_{Ext,i}(\iota, m_i, \lambda)$ and the backscatter efficiency $Q_{Back}(\iota, m_i, \lambda)$ for every aerosol component with refractive index m_i, LR can be calculated:

$$LR = \frac{\sum_{i=1}^{M} \int_0^\infty Q_{Ext,i}(\iota, m_i, \lambda) \cdot \pi \iota^2 n_i(\iota) \mathrm{d}\iota}{\sum_{i=1}^{M} \int_0^\infty Q_{Back,i}(\iota, m_i, \lambda) \cdot \pi \iota^2 n_i(\iota) \mathrm{d}\iota}, \tag{22}$$

where ι denotes the particle radius, M the number of aerosol components, λ the wavelength and n_i the lognormal distribution of each component [Ackermann, 1998]. The numerator represents the extinction contribution α_{aer} and the denominator the backscatter contribution β_{aer} leading to a shorter expression of the lidar ratio, which is already stated in equation 12.

In the region, where the PSA is located, saharan dust events occur around 20 times per year, usually in the summer months from July to September [Guerrero-Rascado

et al., 2008]. Factors that influence the classification of the aerosol type for the elastic LIDAR measurements performed at the PSA are the proximity to the sea and urban area and the saharan and local dust. Müller et al. (2007) determined the lidar ratio for urban haze in central europe as 58 ± 12 sr, for desert dust with source region Sahara 55 ± 6 sr for the 355 nm wavelength. For the 532 nm wavelength the LR for urban haze is given with 53 ± 11 sr, for saharan dust depending on the measurement campaign 55 ± 5 sr and 59 ± 11 sr. Additionally, for marine aerosols lidar ratios between 20 sr and 38 sr have been found [Müller et al., 2007]. According to Guerrero-Rascado et al. (2008), lidar ratios may vary by 20 sr during days with strongly changing weather conditions. Other studies with a special focus on the relative humidity have been carried out by Ackermann (1998) where it was distinguished between the maritime, desert and continental aerosol type and the 355 nm, 532 nm and 1064 nm wavelength. When assuming a relative humidity of 56.6%, as measured as the mean value with the *Campbell Scientific CS* 215 Sensor for the year of 2012 at the PSA, the lidar ratios for the different aerosol types can be obtained from the data published by Ackerman (1998). The values of the LR for the different aerosol types are listed in table 1.

LR	Continental, sr	Desert, sr	Maritime, sr
355 nm	59 ± 4	43 ± 1	23 ± 5
532 nm	58 ± 3	21 ± 2	28 ± 2
1064 nm	45 ± 5	17 ± 1	50 ± 1

Table 1: *Lidar ratios for different aerosol types [Ackermann, 1998].*

With respect to Müller et al. (2007) and Ackerman et al. (1998), for the following considerations a lidar ratio of 58 sr was approximated for the 355 nm wavelength, 55 sr for the 532 nm wavelength and 45 sr for measurements with the 1064 nm wavelength. The ratios were held constant during all measurements and height dependency was neglected. The lidar ratios will be specified in section 4.1.2, where the Klett method is analyzed for its sensitivity regarding the lidar ratio.

2.5.3 Background Correction

Another factor that influences the correct application of the Klett-Fernald method is the background correction. In addition to the scattered photons of the laser, photons from solar radiation during daytime reach the receiver, resulting in an increase of signal magnitude. As stated in section 2.5, the raw signal is range corrected, meaning that it is multiplied with the square of the range where the scatter event took place. If no background correction is made, the signal would consist of the backscatter signal from the photons emitted by the laser and in addition the photons from the solar background radiation. The range correction would then amplify this erroneous signal. Therefore a background correction needs to be applied. Since the background correction is time independent, it is the same for all range-bins and can be subtracted beforehand. This approach is discussed in section 4.1.3.

2.6 Theory - Overlap Problem

Lidar Geometry

A reduction of the backscatter signal in the region of incomplete overlap is due to the geometrical construction of a biaxial LIDAR system. This loss of signal in a region of interest is referred to as the overlap problem. The vertical axis of the receiver differs from the vertical axis of the laser. The light cone emitted by the laser and the field of view of the receiver, where backscattered photons are detectable, are not overlapping at ground height, see figure 1. Only when both regions coincide entirely the detector response to the return signal is not reduced [Stelmaszczyk et al., 2005].

To reduce this geometrical compression, a correction function has to be found to correct the loss of signal for the region of incomplete overlap. For the LIDAR system located at the PSA, the altitude of complete overlap is 120 m, which is comparatively low [Stelmaszczyk et al., 2005, Biavati et al., 2011]. Also other factors, such as the presence of obstacles inside the telescope and insufficient size of a detector can contribute to the geometrical compression. Three different approaches to deduce a correction function are discussed in detail in the following sections. The first method is entirely based on numerical assumptions, the second uses multi-angle measurements and the third uses the ceilometer data as reference.

Furthermore, there is a great variety of other approaches, relying on different presumptions or measurement methods. For example the technique proposed by Wandinger and Ansmann (2002), which is based on the measurement of a pure molecular backscatter signal in addition to the elastic backscatter signal performed with a Raman LIDAR. The underlying principle is that the overlap profiles for the elastic backscatter and the Raman channels are identical. It is then possible to deduce the lidar overlap profile iteratively for altitudes smaller than the complete overlap region [Wandinger and Ansmann, 2002]. An alternative overlap correction method using a secondary receiver is proposed by Berkoff et al. (2003). The secondary receiver is co-aligned and has a ≈ 20 times larger field of view than the primary receiver. Therefore, it reduces its overlap range, but also suffers from a high signal-to-noise ratio (SNR). Taking the ratio of the two measurements into account and applying a scaling factor which accounts for the difference in efficiencies of the receivers, it yields the correction function [Berkoff et al., 2003]. In the following sections the approaches for the determination of the correction functions are discussed. The methods are based on geometrical considerations and measurements with the elastic LIDAR system and the ceilometer.

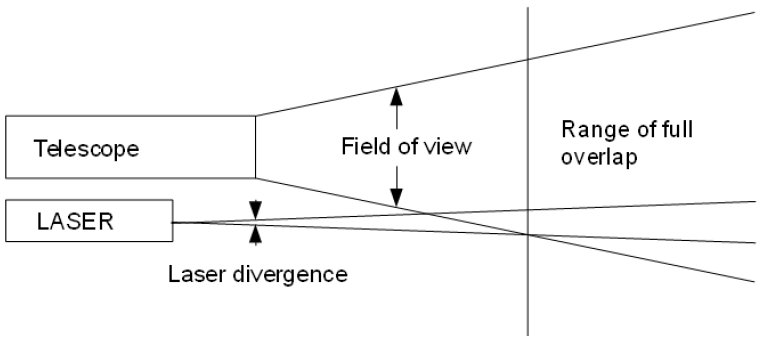

Figure 1: *Simplified scheme of the overlap problem [Groß, 2011].*

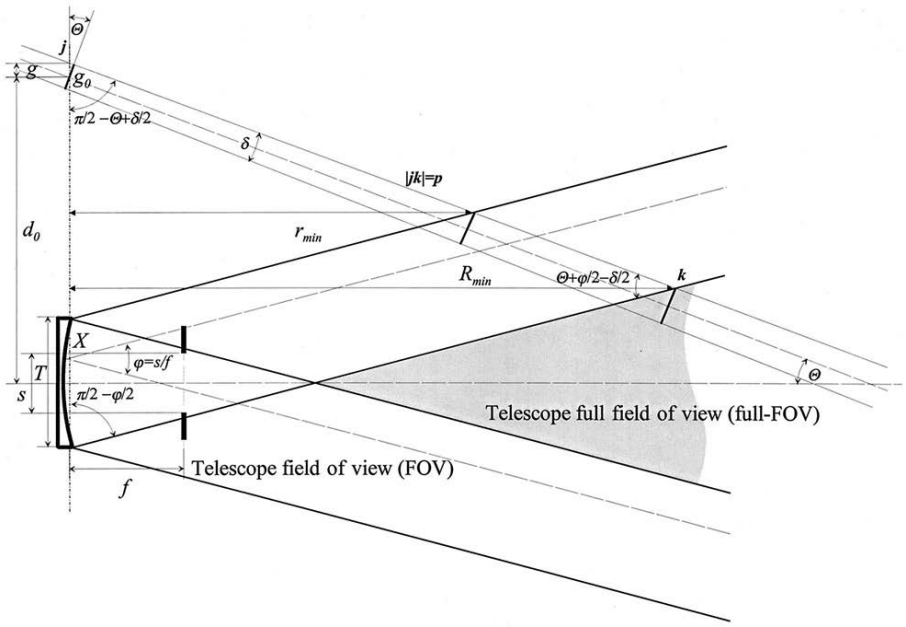

Figure 2: *Detailed scheme of the overlap problem indicating the quantities that have to be known for a determination of the correction function [Stelmaszczyk et al., 2005].*

2.7 State of the Art - Overlap Problem

2.7.1 Analytical Correction Function

To overcome the incomplete overlap problem Stelmaszcyk et al. (2005) proposed a correction function, which is solely based on geometrical considerations. This approach differs from the correction function firstly proposed by [Kuze et al., 1998], where also biaxial lasers were considered with parallel orientation of the telescope and the laser. Since this assumption cannot be verified during measurements, a small inclination angle between the receiver and transmitter has to be assumed. It is impossible to determine the inclination angle from measurements, so that specifications of the system provided by the manufacturer are needed.

To deduce the important parameters from analysis of lidar signals the LIDAR equation is applied. For conformity, parameter notations used by Stelmasczyk et al. (2005) are modified.

$$P(r) = P_0 \frac{c\tau}{2} A\epsilon \cdot \frac{O(r)}{r^2} \cdot \beta(r) \cdot \exp\left(-2\int_0^r \alpha(r)\mathrm{d}r\right).$$

The correction function is denoted $O(r)$ and stands for the ratio of energy transferred to the photodetector E_{det} to the energy reaching the telescope primary mirror E_{scat}.

If the correction function $O(r)$ approaches values close to 1, a major part of the light is focussed inside the detectors sensitive area. A full overlap is accomplished at the full-overlap distance, leading to a correction function that equals to 1. Supposing a laser beam with ideal circular shape is emitted into the atmosphere at an inclination angle θ with respect to the receiver axis, the full-overlap distance R_{min} can be determined

using:

$$R_{min} = p \cdot sin\left(\frac{\pi}{2} - \theta + \frac{\mu}{2}\right), \tag{23}$$

where p is defined as:

$$p = \left(\frac{T}{2} + d_0 + g\right) \cdot \frac{cos\left(\frac{\phi}{2}\right)}{sin\left(\theta + \frac{\phi}{2} - \frac{\mu}{2}\right)}. \tag{24}$$

The distance between the laser beam exit and the receiver is d_0 and the initial beam diameter is g_0. To avoid double occupancy of greek terms, the notation of the laser beam divergence as indicated as δ in the scheme 2 is changed to μ in the description. Also the notation of the primary mirror diameter T is changed to the alternative notation D. ϕ is the telescope's field of view and s and f correspond to the aperture and the focal length of the telescope, respectively. According to Stelma et al. (2005), it has an immense impact to differentiate between the FOV and the full-FOV. The full-FOV refers to the region, in which the backscattered light will be completely focussed onto the sensitive area of the detector, while the FOV also includes regions where backscattered light is focussed outside aperture s. Due to the small scale sizes of the laser beam divergence μ, see δ in figure 2, in the order of 1 mrad and its inclination angle $\theta < 0.25$ mrad, it is satisfactory to combine equation 23 and 24 to determine the full-overlap distance [Raymetrics, 2012, Stelmaszczyk et al., 2005]:

$$R_{min} = \frac{2d_0 + g_0 + D}{s\theta + \phi - \mu}. \tag{25}$$

The area of illumination inside the telescope's full FOV can be expressed with:

$$e(r) = f\left(\mu + \frac{g_0 + D}{r}\right), \tag{26}$$

always assuming the telescope's full FOV cannot be smaller than the laser beam's divergence. Given an object G, by which light is scattered, a small displacement depending on the inclination angle θ has to be taken into account. This displacement results from a shift of arbitrary size of the object from the telescope's axis and is equal to:

$$\nu(r) = f\frac{d_0 - \theta r}{r}. \tag{27}$$

To deduce the correction function, geometrical observations can be applied. Assuming an energetically uniform distributed laser beam scattering by an object, the total energy reaching the primary mirror is proportional to the image area. Also the energy transferred to the photo detector is proportional to the overlap between the aperture and image. Other energy losses are due to energy transmission losses in air. Thus, one can rewrite the correction function as:

$$O(r) = \frac{E_{det}}{E_{scat}} = \frac{F(r)}{\pi\left[\frac{e(r)}{2}\right]^2}, \tag{28}$$

where the numerator $F(r)$ corresponds to the overlap area and the denominator to the circular sector area, respectively [Stelmaszczyk et al., 2005]. Defining the angles:

$$\Psi_1(r) = \left\{ 2 \; arccos \left[\frac{s^2 + 4\nu^2(r) - e^2(r)}{4\nu(r)s} \right] \right\}, \tag{29}$$

$$\Psi_2(r) = \left\{ 2 \; arccos \left[\frac{s^2 + 4\nu^2(r) - s^2}{4\nu(r)e(r)} \right] \right\}, \tag{30}$$

a form of the correction function can be derived as:

$$O(r) = \frac{\{\Psi_1(r) - sin\left[\Psi_1(r)\right]\} s^2 + \{\Psi_2(r) - sin\left[\Psi_2(r)\right]\} e^2(r)}{2\pi^2(r)}. \tag{31}$$

Because so far the correction function 2.7.1 does not hold for special cases namely the condition where full overlap or in contrary no overlap is achieved, the following modification for any arbitrary distance R from the LIDAR system must be extended to:

$$O(r) = \begin{cases} 0 & \nu(r) \geq s + e(r)/2 \\ \frac{\{\Psi_1(r) - sin[\Psi_1(r)]\} s^2 + \{\Psi_2(r) - sin[\Psi_2(r)]\} e^2(r)}{2\pi^2(r)} & |s - e(r)|/2 < \nu(r) < s + e(r)/2 \\ \frac{s^2}{e^2(r)} & \nu(r) < [e(r) - s]/2, \quad e(r) > s \\ 1 & \nu(r) < [s - e(r)]/2, \quad e(r) \leq s \end{cases}. \tag{32}$$

Compared to the correction functions achieved via experimental approaches, the correction function proposed by Stelma et al. (2005) lies within a maximum error region of 10 %. The analytical approach results in a sharp, step-like change in the correction function in the region, where the laser beam enters the telescope's FOV, which can not be verified by measured data [Stelmaszczyk et al., 2005]. Therefore, a non-homogeneous energy distribution within the laser beam is assumed and lies in good accordance with the commonly known suggestion of a Gaussian profile of the laser beam [Stelmaszczyk et al., 2005].

2.7.2 Correction Function by Multi-angle Measurements

Biavati et al. (2011) proposed a solely experimental technique for the correction of the incomplete overlap with the advantage that there is no need of knowing all exact parameters, such as the inclination angle of the laser or the laser beam divergence, which may be the subject of uncertainties from the system. For close ranges from 10 m to a few hundred meters the correction function can be retrieved iteratively using data recorded from vertical and angular measurements, assuming horizontal homogeneity of the area close to the instrument [Biavati et al., 2011]. This method can also be implemented for portable LIDAR systems that can be oriented at different angles beside 90° and are optically and mechanically stable during operation [Biavati et al., 2011]. The elevation angle ω for the angular acquisition specifies the altitude at which the signal can be corrected. The smaller the elevation angle, the lower is the altitude for which a signal correction is possible. Prerequisite for this approach is that both profiles yield the same values in the full overlap region. It is assumed that the vertical

stratification of the atmosphere remains constant over the time of two consecutive measurements. In principle, the profile taken at the smaller elevation angle samples the same stratified atmosphere, reaching the region of complete overlap at a lower altitude with respect to the vertically measured backscatter profile [Biavati et al., 2011]. According to Biavati et al. (2011), the backscatter profile for the vertical measurement can be progressively reconstructed down to the minimum sampling altitude, acquired with the lower elevation angle. Considering two consecutive measured raw backscatter signals that are range corrected and a function of r, where $X_2(r)$ is the signal from vertical measurement and $X_1(r)$ from measurement with an elevation angle $\omega < 90°$, in general holds:

$$X_2(r) \begin{cases} < X_1\left(\frac{r}{sin\ \omega}\right) & \text{for } r < R_{min} \\ = X_1\left(\frac{r}{sin\ \omega}\right) & \text{for } r \geq R_{min} \end{cases}. \tag{33}$$

The first correction factor that is used to correct X_2 is:

$$\Gamma_1(r) = \frac{X_1\left(\frac{r}{sin\ \omega}\right)}{X_2(r)} \tag{34}$$

and consequently the second correction is:

$$\Gamma_2(r) = \frac{X_1\left(\frac{r}{sin\ \omega}\right)\Gamma_1\left(\frac{r}{sin\ \omega}\right)}{X_2(r)} = \frac{X_1\left(\frac{r}{sin\ \omega}\right)X_1\left(\frac{r}{sin^2\ \omega}\right)}{X_2(r)X_2\left(\frac{r}{sin\ \omega}\right)}. \tag{35}$$

According to equations 34 and 35 a generalization of this correction procedure for n iterations can be written in the most convenient form:

$$\Gamma_n = \frac{X_1\left(rsind^{-n-1}\ \omega\right)}{X_2(r)} \prod_{i=1}^{n} \frac{X_1\left(rsin^{-i}\ \omega\right)}{X_2\left(rsin^{-i}\ \omega\right)} = O(r). \tag{36}$$

Applying the correction function $O(r)$ to the unmodified vertical data, the range of exploitation of the lidar signal can be reduced to approximately 100 m [Biavati et al., 2011].

2.7.3 Correction Function with Ceilometer as Reference

Another experimental method to retrieve the correction function for LIDAR measurements is proposed by Guerrero-Rascado et al. (2010). The fundamental idea that underlies this approach is the deviation between the elastic lidar profile and the ceilometer profile. The ceilometer's receiver has a bigger FOV than the receiver of the LIDAR system, resulting in a smaller full-overlap distance $R_{min,ceilo}$. Furthermore, the ceilometer profile is already corrected for the region of incomplete overlap by an internal correction function and therefore allows for retrieving the lidar overlap correction function. An *iterative method* and a *direct method* are presented, both relying on the ceilometer attenuated backscatter coefficient as a reference. The elastic LIDAR equation, stated in section 2.3, can be simplified to [Guerrero-Rascado et al., 2010]:

$$P(r) = \frac{K \cdot O(r)}{r^2} \cdot \beta(r) \cdot T^2(r), \tag{37}$$

where $P(r)$ is the backscattered laser power, K is a system constant that includes all range independent instrumental parameters, such as the detector's efficiency, the laser

pulse width or the telescope's diameter and $O(r)$ is the correction function. $\beta(r)$ is the volume backscatter coefficient that gives together with the atmospheric transmittance $T(r)$, information about the extinction of light due to particles or molecules in air between the instrument and the altitude of scattering. Both parameters can be rewritten to the more convenient form, as already stated in section 2:

$$\beta_{att}(r) = \beta(r) \cdot T^2(r).$$

β_{att} refers to the total attenuated backscatter coefficient, which is composed of the molecule and aerosol backscatter coefficient and the square of the transmittance $T(r)$. The total attenuated backscatter coefficient provided by ceilometer measurements is practically unaffected by the incomplete overlap effect, due to the ceilometer's bigger FOV, and can therefore be used as a reference for the aerosol backscatter coefficient in the lowest altitudes of the lidar signals, which need to be corrected. The aerosol backscatter coefficient is obtained by applying the Klett-Fernald method to the LIDAR data, as described in section 2.5. Subsequently the lidar backscatter profiles can be converted into attenuated backscatter profiles [Guerrero-Rascado et al., 2010, Mona et al., 2007]. The following subsections describe the two approaches proposed by Guerreo-Rascado et al. (2010). The measured signal is averaged for 30 min and includes a source of error in the correction functions due to non-negligible variation of aerosol loads in the atmosphere.

Iterative Method In order to compare both profiles, the ceilometer attenuated backscatter profile must be scaled to the lidar wavelength. This conversion factor is found to be the ratio of the mean value of the lidar and ceilometer profile in a region of full overlap, typically above 2.5 km, where both signals show a constant behavior for clear atmospheres [Guerrero-Rascado et al., 2010]. The *iterative method* is based on two proportionalities. Firstly, the elastic lidar signal is after range correction and overlap correction proportional to the ceilometer attenuated backscatter profile $\beta_{attenuated,ceilom,unaffected}$, which corresponds to the elastic ceilometer signal after range correction and multiplication with the transmittance term as stated in equation 3 [Guerrero-Rascado et al., 2010]:

$$\beta_{attenuated,ceilom,unaffected}(r) \sim P(r) \cdot r^2 \cdot O^{-1}(r), \tag{38}$$

with $P(r) \cdot r^2$ being the range corrected backscatter signal and $O^{-1}(r)$ is the correction function of the LIDAR. Secondly, the elastic lidar signal after range correction is proportional to the lidar attenuated backscatter profile $\beta_{attenuated,lidar,affected}$:

$$\beta_{attenuated,lidar,affected}(r) \sim P(r) \cdot r^2. \tag{39}$$

The relative difference $\Delta O(r)$ is used to reduce iteratively the effect on the elastic lidar signal and is defined as:

$$\Delta O(r) \equiv 1 - O(r) = \frac{P(r) \cdot r^2 \cdot O^{-1} - P(r) \cdot r^2}{P(r) \cdot O^{-1}} \sim \frac{\beta_{attenuated,ceilom}(r) - \beta_{attenuated,lidar}(r)}{\beta_{attenuated,ceilom}(r)}. \tag{40}$$

For the first step, $i = 1$, the uncorrected elastic lidar signal is used to obtain $\Delta O^{(1)}(r)$ and the lidar attenuated profile with:

$$\Delta O^{(i)}(r) = \frac{\beta_{att,ceilom,unaffected}(r) - \beta^{(i)}_{att,lidar,affected}(r)}{\beta_{att,ceilom,unaffected}(r)} \tag{41}$$

and:

$$P^{(i+1)}(r) = P^{(i)}(r) \cdot \left[1 + \Delta O^{(i)}(r)\right]. \tag{42}$$

The relative difference obtained with equation 41 is then inserted into equation 42 to correct the lidar backscatter signal. With the Klett method the attenuated backscatter coefficient can be calculated and then used again for determination of ΔO. Further steps are achieved by repeated application of this method, correcting the signal stepwise. The correction function is then given by:

$$O(r) = \frac{P^{(1)}(r)}{P^{(end)}(r)}. \tag{43}$$

According to Guerrero-Rascado et al. (2010), 20 to 25 iterations are sufficient to remove the effect of incomplete overlap completely. The corrected lidar attenuated backscatter coefficient is proportional to the ceilometer attenuated backscatter signal.

Direct method A faster determination of the correction function is the *direct method*. Advantageous for this approach is that an explicit scaling of the ceilometer profiles to the lidar profiles is not needed. The correction function contains an unknown constant L, which includes the scaling factor and also the relative difference of the ceilometer attenuated profile and lidar attenuated profile, yielding the shorter form:

$$O(r) = \frac{P(r) \cdot r^2}{L \cdot \beta_{att}}. \tag{44}$$

L is chosen such that $O(r)$ smoothly tends to 1 for the complete overlap region [Guerrero-Rascado et al., 2010].

3 Methods

Figure 3: *METAS at the Plataforma Solar de Almería.*

In this section the experimental methods for data acquisition using the LIDAR, the ceilometer and the sun photometer are described. All three instruments are located at the Meteorological Station for Solar Technologies (METAS), see figure 3, in distance of 5 m and hence are especially suited for a comparison of simultaneous measurements. LIDAR and ceilometer measurements were carried out to determine the aerosol extinction coefficient. The according AODs can be derived from the data. Sun photometer measurements also yield information about the AOD. Therefore sun photometer, LIDAR and ceilometer data can be intercompared. Moreover, the LIDAR system provided by Raymetrics is tiltable, covering elevations from 0 - 90° and therefore allows the implementation of the correction function proposed by Biavati et al. (2011) from angular measurements. In addition, LIDAR and ceilometer data is used for the implementation of the correction function proposed by Guerrero-Rascado et al. (2010), described in section 2.7.3. Furthermore, the corresponding data processing will be specified in this section.

3.1 LIDAR

3.1.1 Components

Laser The active source in the LIDAR setup is the solid state Nd:YAG (neodymium-doped yttrium aluminium garnet) laser. YAG ($Y_3Al_5O_{12}$) is the host material, which is doped with the rare earth element neodymium to create active laser ions. Via frequency multiplication the YAG crystal generates through double refraction the second and third harmonic frequencies. This process is called "Second harmonic generation". The Nd:YAG laser emits simultaneously light pulses of 355 nm, 532 nm and 1064 nm wavelength. The laser pulses pass through a chamber with optical elements, as shown in figure 4 and 5(b). The optical set-up consists of mirrors and splitters that account for laser beam transportation and time synchronization. For laser beam transportation,

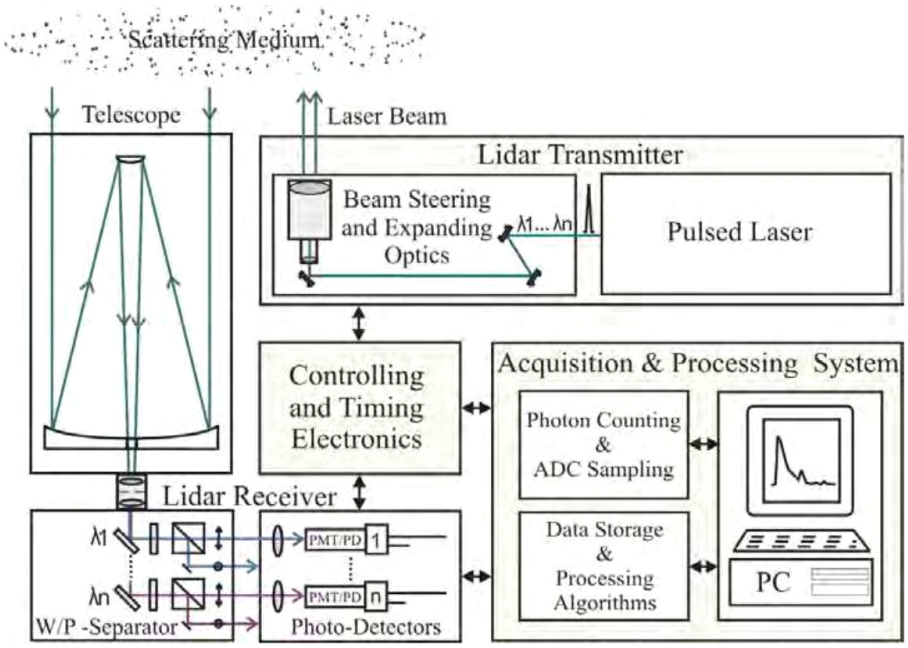

Figure 4: *General block schematic of the LIDAR setup [Stoyanov et al., 2012].*

an expanding telescope is installed, that minimizes the output beam divergence. Mechanical mounts with precise translation and rotation mechanisms account for beam steering and LIDAR adjustment [Stoyanov et al., 2012]. The distance between the transmitter and receiver is 24.687 cm. More specifications of the laser are given in table 2.

Receiver As receiver for the backscattered photons a Dall-Kirkham Cassegrain telescope is used, see figure 5. Telescopes of the type Cassegrain contain a primary concave mirror and a secondary convex mirror. Both are aligned to collect and focus the light through a hole in the center of the primary mirror onto the detection unit placed on the telescope's focal point [Raymetrics, 2012]. The special feature of a Dall-Kirkham telescope are the differently shaped mirrors. The primary concave mirror is elliptical while the secondary mirror is spherical, causing an easier focusing for the on-axis field of view and a quickly degrading when off-axis. The diameter of the telescope's primary mirror is 30 cm, its focal length is 1500 mm. The FOV of the telescope is $\phi = 0.001$ rad. Both, the primary and the secondary mirror are coated with a durable high reflective coating, suitable for the $350-1064$ nm spectral region [Raymetrics, 2012]. After passing through the entrance pupil of the telescope the backscattered light is guided through

Emitted wavelengths	355 nm, 532 nm, 1064 nm (collinear)
Total Energy per pulse	400 mJ/pulse
Pulse duration	$7-9$ ns
Repetition rate	20 Hz
Beam diameter	7 mm
Laser beam divergence	< 0.25 mrad (after laser beam expansion)

Table 2: *Specifications of the Transmitter [Raymetrics, 2012].*

(a) (b)

Figure 5: *(a) Laser and telescope of the transportable LIDAR system located at the PSA, Tabernas, Spain. The image shows the system in a 20° elevated position. (b) Chamber with opto-mechanical elements for beam steering. This chamber is located on top of the laser and controls the beam exit.*

a mirror system, see figure 4, with spectrally selective elements that transmit less than 4 - 10% in the blocking spectral regions [Stoyanov et al., 2012]. Beam splitters separate the wavelengths of the backscattered laser radiation, forming detection channels as indicated in the block schematic in figure 4. As a result the elastic wavelengths can be detected with a good signal-to-noise ratio promoting also weak signals from high altitudes of the lidar sounding path [Stoyanov et al., 2012]. The LIDAR system installed at the PSA is equipped with 355 nm, 532 nm and polarized 532 nm detection channels.

Detection unit The detection unit consists of an analog-to-digital converter and a photomultiplier tube. The selected optical lidar signals are converted to electrical signals with a conversion rate of 12-16 bit at 20 MHz with a 250 MHz fast, highly-sensitive photon counting system. The raw spatial resolution is selectable with the minimum resolution of 7.5 m and the raw signal range is given from 120 m up to 120 km [Raymetrics, 2012]. The minimum raw temporal resolution is 10 seconds for multiple acquisition mode. The detector has two operational modes, analog and photon counting with a full-width-half-maximum (FWHM) detection bandwidth of ≈ 0.5 nm for the 532 nm polarized and unpolarized wavelengths and ≈ 1.0 nm for the 355 nm wavelength. The detector operates parallely in analog (AN) and photon counting (PC) mode. Analog signals are usually used when the incident light intensity is great and the SNR small, so that signal peaks extend to the whole scale of detectable intensity without being saturated. Weak signals, usually detected at high ranges, are amplified using a photomultiplier tube (PMT) and are referred to as photon counting signals. The acquisition and processing system, as indicated in figure 4, provides software based sampling,

processing and storage of the acquired lidar profiles, applying specialized retrieving algorithms [Stoyanov et al., 2012]. The transmitter and receiver of the LIDAR system operate fully controlled and synchronized by the controlling and timing electronics.

3.1.2 Alignment

Before a measurement is started, system calibration should be performed, to check if the system is aligned properly. The backscattered photons that reach the telescope hit the detector using different paths and with different incident angles [Freudenthaler, 2008]. If the system is misaligned, only fractions of the backscatter signal can be detected. In figure 6 a misaligned system is sketched, where the laser beam exits the field of view of the telescope.

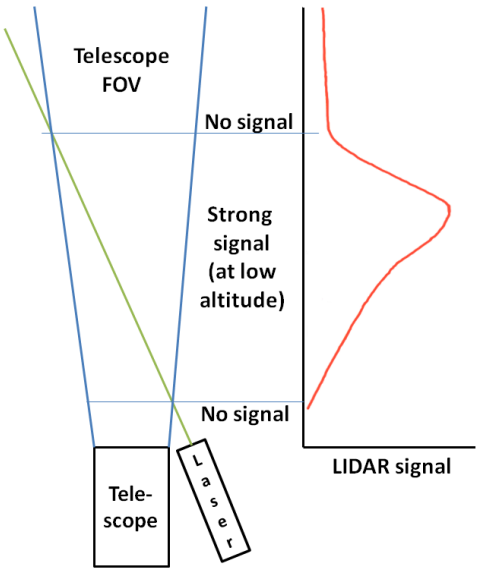

Figure 6: *Misaligned LIDAR system.*

Rayleigh Calibration For checking the alignment, a data set of an elastic backscatter signal is used which is measured at a clear period without clouds, where contiguous 5 min corresponding to 3000 laser shots are sufficient. The data of the analog and the photon counting signal need to be averaged. Assuming that the atmosphere is clear, meaning only molecular scattering takes place, beginning in a region between 5000 m and 7000 m, the alignment can be checked by monitoring the normalized molecular backscatter coefficient β_{mol} and the normalized range corrected lidar signal RCS from the analog data. A normalization is needed, so that both profiles lie in the same frame. If both profiles show a good fit in the region from 5000 m to 7000 m, the LIDAR system is well aligned. The same procedure needs to be done for the photon counting signal, because the analog signal is not valid above 7000 m to 9000 m due to the high SNR. Alternatively, analog and photon counting data could be glued beforehand, see details in section 3.1.5, instead of comparing analog and photon counting signals separately.

Telecover test A faster method to check the alignment of the LIDAR system is the telecover test. For this test, a circular paper with the dimensions of the telescope window is used. One quarter is cut out of the paper, such that the paper covers the telescope window and just quarters can be used for measurement. When the paper is rotated, so that the open quarter is pointing to the laser, the signal should have a peak at 180 m, where the full overlap range begins for the uncorrected raw analog signal. The signal intensity should be $\frac{1}{4}$ of the possible signal intensity if no area would be covered. Small motors serve to correct the inclination angle of the laser towards the receiver. When the open quarter is pointing to each side, the same signals should be achieved. In case both quadrants yield different signals, the laser is tilted to the side, away from the laser-receiver axis, and needs to be corrected. Generally, when the open quarter is opposite to the laser, the peak indicating full overlap should be in farther range [Freudenthaler, 2008].

3.1.3 Data Collection

After the alignment procedure has been performed, the data acquisition can be started. The acquisition interface allows a change of time resolution and bin size. A lidar profile is derived from an average of a greater number of laser pulses. Depending on how the transient recorder is configured, the profiles will be averaged automatically. The minimum value for automatic operation is 20 laser shots and the maximum is 4095, corresponding to 3.4 min that can be averaged. However, even single shots are possible through manual operation of the LIDAR [Raymetrics, 2012]. According to Abdullah et al. (2013), a time period of 1 min is sufficient to eliminate artifacts caused by background noise from the signal [Abdullah et al., 2013]. For the purpose of comparison to other instruments, such as the sun photometer and the ceilometer, a time resolution of 1 min is suitable, as fast changing weather conditions can still be detected. With a laser pulse frequency of 20 Hz, 1201 laser pulses are emitted during 1 min. Therefore, a time resolution of 1 min was chosen for measurements performed in this thesis. Also the bin size is selectable and set to 7.5 m to ensure the highest possible spatial resolution. Thus, 1 range bin corresponds to 7.5 m. The maximum range is 120 km, although, known from experimental experience the signal above 15 km does not contain information due to the high signal-to-noise ratio. For data analysis the Raymetrics software including Licel software for controlling and processing is used. A MATLAB routine was implemented to derive the aerosol extinction coefficient including on-site measurements for pressure and temperature and the raw signal of the LIDAR. Data corresponding to a time period of 33 h and 32 min has been collected between the 2013/08/01 and the 2014/06/11. 22 h and 18 min of this data were measured at clear atmospheric conditions and approximately 1 h was dedicated to angular measurements. The data from the vertical measurements serves for comparison to ceilometer and sun photometer data. Measurements performed at cloudy or hazy conditions are solely for comparison to ceilometer data and the determination of the aerosol extinction coefficient. The 355 nm, 532 nm and polarized 532 nm channels detect a purely backscatter signal from elastic backscattering events. The backscatter signals at 355 nm and 532 nm are analyzed with respect to the derivation of the aerosol extinction coefficients.

3.1.4 Data Processing

For post processing of the data a LabVIEW Post Processing Software is provided by Raymetrics that allows data preview and analysis. From the database a data set can be chosen for data export. Signals from 355 nm, 532 nm and polarized 532 nm channels are available for pre-analysis. With respect to each wavelength it can be differentiated between analog and photon counting signals which can either be saved together for export or separately in an ASCII file. The program additionally offers a background correction and gluing tool. The background correction tool allows a subtraction of the mean signal from a selectable range, chosen in the far-end region above 14.5 km, where the SNR is high and signals are weak. For the purpose of deeper understanding of the gluing process, a MATLAB routine based on the LabVIEW Software was implemented, as later discussed in section 3.1.5 and gluing was performed externally.

The LabVIEW Software for data acquisition program controls the system and processes data of the experiment, requiring the data export right after a measurement. The Licel control modules, included in the LabVIEW structure, are the transient recorder,

the high voltage photomultiplier, the high voltage APD (Avalanche Photodiode) and the trigger based on ASCII (American Standard Code for Information Interchange) command sets [Licel, 0011]. The transient recorder ethernet control module translates the ASCII based commands into low level transient recorder commands, which then can be sent back to the PC [Licel, 0011]. The control voltage of the PMT is generated by a precise digital-to-analog-converter (DAC) and ranges between 0 and 1 V. The Licel APD high voltage control module is also controlled by a precision DAC with a control voltage ranging from 0 to 1.8 V. Both voltage controls can be monitored on the PC. To synchronize the system, the trigger module is used that is coupled to a quarz based oszillator ensuring nanosecond timing stability.

3.1.5 Analog and Photon Counting Signal

The LIDAR detector captures backscatter signals that can span a dynamic range of up to 5 orders of magnitude. To exploit the return power signal with a high sensitivity for all magnitudes, the Licel transient recorder TR 20 160 operates in a dual acquisition mode. The backscatter signal is simultaneously converted with the analog-to-digital and photon counting mode [Lange et al., 2011]. For the following considerations the analog and photon counting signal are referred to as AN and PC, respectively. Although both data sets can be analyzed separately, a combination of the signals offers great advantages. For high level signals the AD conversion is of high linearity, especially for close ranges up to 7 km. The PC mode is highly sensitive for low level signals, usually obtained from greater distances [Lange et al., 2011]. To obtain exact information about the atmospheric conditions, the backscatter signal must reveal a high sensitivity at all ranges. Hence, a combination (gluing) of the analog and photon counting signal has been aimed.

Gluing is possible in a region where both signals are valid and reveal the same atmospheric conditions [Mielke, 2005]. This preposition is fulfilled when both signals demonstrate the same physical properties, meaning that the raw backscatter signal increases or decreases with the same gradient. The gluing region extends typically from 2 to 50 MHz in the photon counting mode. The glued signal then is used for further evaluations. The gluing algorithm includes the following steps: 1. Dead time correction, 2. Bin Shift Correction and 3. Determination of Gluing Parameters.

Dead Time Correction A systems dead time corresponds to the short time period right after a discrete scattering event was recorded and during which the system is not able to record another event. There are in general two types of systems for which a dead time correction of the photon counting data is applicable: the paralyzable and the nonparalyzable systems. For the paralyzable system the photon counting signal can be corrected using:

$$N = S \cdot \exp(-S\tau_t), \tag{45}$$

where N is the observed count rate, S the true count rate and τ_d the system's dead time [Mielke, 2005]. The Licel photon counter can be best described by the nonparalyzable System. For that case the dead time corrected photon counting signal is given by the following equation:

$$S = \frac{N}{1 - N \cdot \tau_d}. \tag{46}$$

According to Raymetrics (2012), the system's dead time τ_d is 260 MHz $\widehat{=}$ 3.8 ns so that the dead time corrected signal S is:

$$S = \frac{N}{1 - N \cdot 3.8} \text{ MHz}. \tag{47}$$

This correction is only valid for lower count rates when $S \cdot \tau_d < 1$ [Mielke, 2005]. Figure 7 shows the dead time corrected photon counting signal and the observed raw photon counting signal measured on 2014/03/05, 12:01 pm for the 355 nm channel.

The signal's dead time correction accounts for the signal loss due to the systems dead time. The maximum intensity of backscatter signal increases by more than 100 %, as can be seen in figure 7 and needs to be applied before further data analysis, as it is essential for a correct data processing.

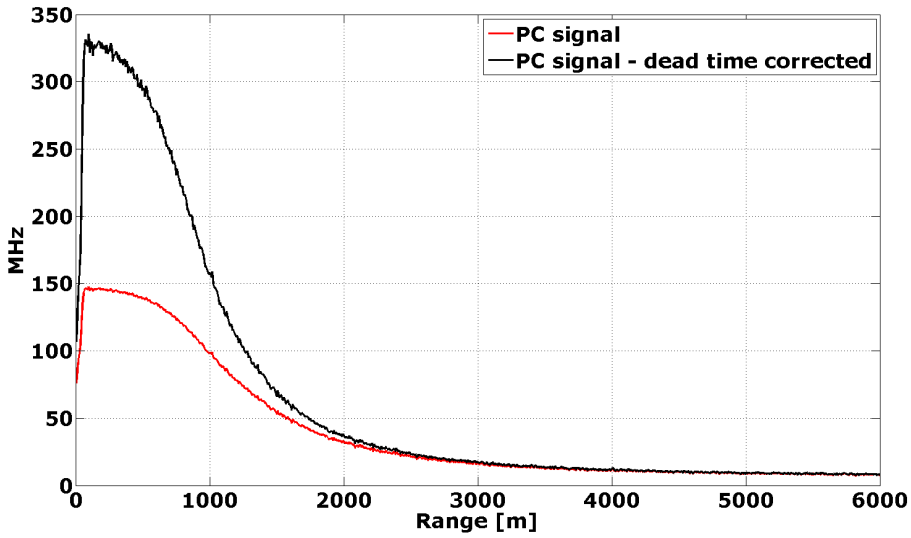

Figure 7: *Raw PC signal (red) and corresponding dead time corrected signal (black) for 355 nm. Recorded on 2014/03/05, 12:01 pm.*

Bin Shift Correction For gluing the analog signal to the photon counting signal, the analog signal has to be scaled according to the photon counting signal. Special attention has to be given to a possible bin shift. This bin shift can be determined from experimental data, when a cloud or aerosol layer is detected with both signal types. The analog signal is shifted by several range bins, indicating the cloud layer at higher ranges with respect to the photon counting signal. The signal shifting appears due to the functioning of the preamplifier of the analog channel. That amplifier contains an anti-alias filter, with a bandpass of half the frequency, that delays the analog signal. As LIDAR is a time-of-flight technique this delay refers to shift in the measured range. Another source of bin shifting is based on the analog-to-digital pipelining. Voltage sampling is a multiple step process providing the sample result several clock cycles after the actual sampling took place [Abdullah et al., 2013, Licel, 0011].

The bin shift varies for each LIDAR system and has to be found experimentally. To obtain the best accordance between the PC and AN signal for the LIDAR system at the PSA, the analog signal was shifted by 9 bins or 255 ns, as can be seen in figure 8. The depicted data were acquired with the 355 nm LIDAR channel on 2014/03/05, 12:01 pm.

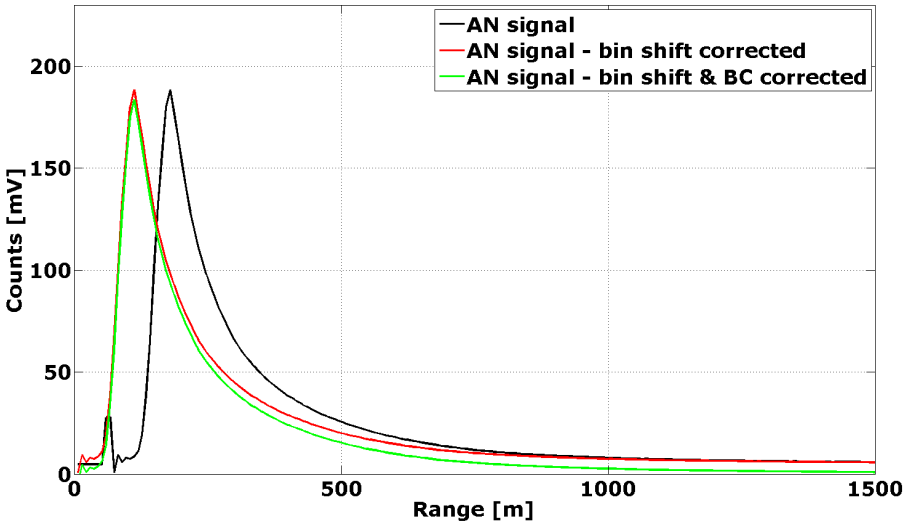

Figure 8: *Raw AN signal for 355 nm (black), bin shift corrected signal (red) and background corrected signal (green). Recorded on 2014/03/05, 12:01 pm.*

Determination of Gluing Parameters To scale the AN signal to the PC signal, linear regression coefficients have to be found in a region where both signals decrease with a similar gradient. The linear regression coefficients a and b are determined with:

$$\sum_{i=1}^{n} \left(PC\left(r_i\right) - \left(a \cdot Analog\left(r_i\right) + b\right)\right)^2 = min. \tag{48}$$

The index i corresponds to the bin number, where the gluing region begins [Lange et al., 2011]. The gluing region is found defining the upper and lower toggle frequencies. The toggle frequency describes the output frequency of the generated signal. As minimum and maximum toggle frequencies 23.34 MHz and 49.69 MHz were chosen, which correspond to memory bin numbers 212 and 285, respectively. This correspondence can be found when comparing with the dead time corrected PC signal. Therefore, the gluing region extends from 1590 m to 2137.5 m and is invariant for all LIDAR measurements. The linear regression coefficients are determined with equation 48. For the displayed data in figure 9(a) and 9(b) the analog signal was background corrected, as can be seen in figure 8. The regression coefficients for this data set were then found to be $a = 67.8$ and $b = 0$. For each measurement the regression coefficients have to be determined separately, as they depend on local atmospheric conditions and system parameters, such as the PMT voltage. The AN and PC signals are separately averaged over the measured time period and the regression coefficients are consistently applied to the complete data set of one measurement cycle. Variations for a and b can be approximated with ± 10 and are seeked with 0.1 accuracy in the MATLAB routine. Finally, the bin shifted and scaled analog signal is glued to the photon counting signal at the bin number 212 or 1590 m. The results of the gluing process can be seen in figure 9(a), where the bin shifted AN signal, the dead time corrected PC signal and the resulting glued signal of the 2014/03/05, 12:01 pm are depicted for the 355 nm wavelength. The gluing parameters have been determined from the whole measurement period between 11:37 am and 15:38 pm. It can be seen that the transition from the PC signal to the scaled AN signal is very smooth and does not cause distortions in the gluing region.

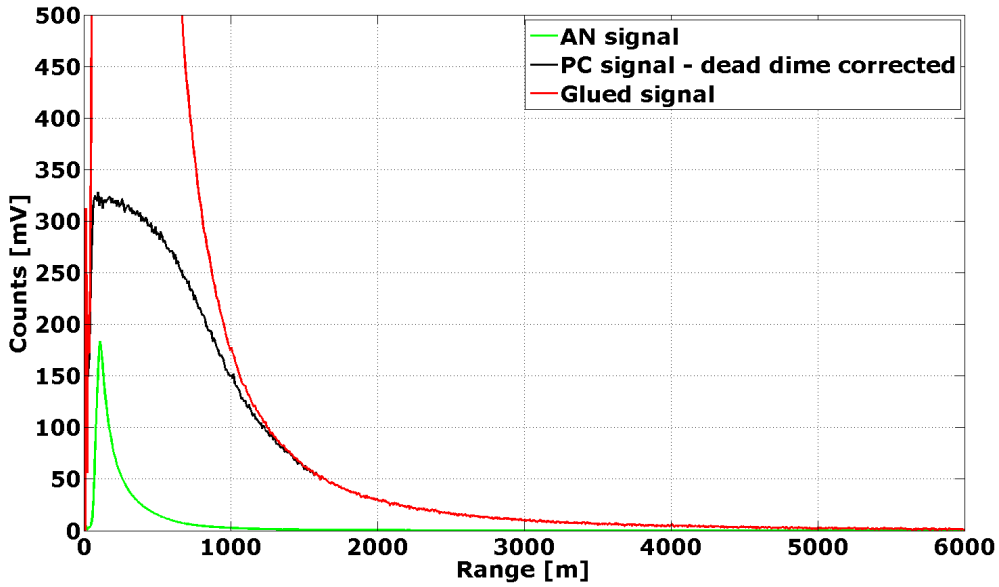

(a)

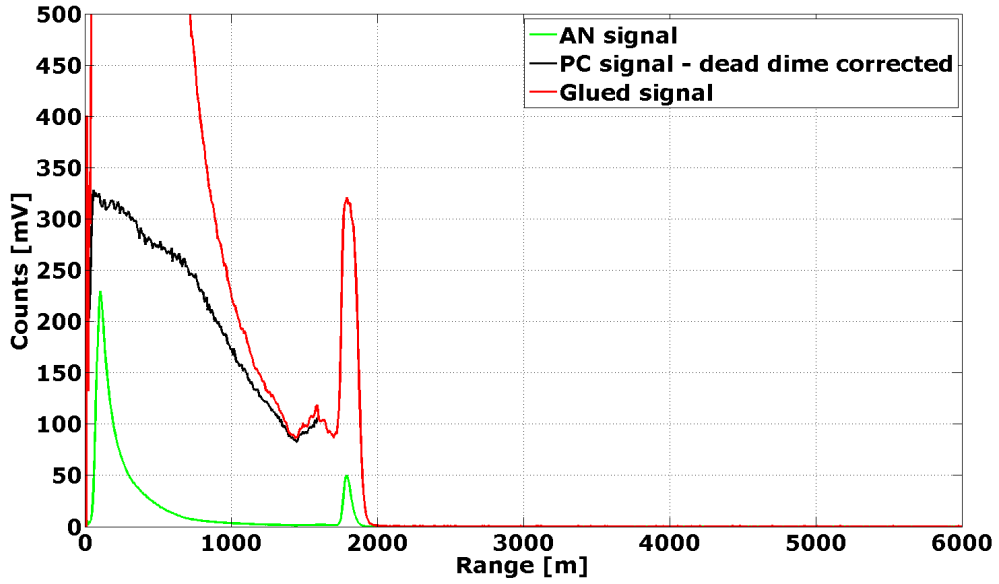

(b)

Figure 9: *(a) Bin shifted, background corrected analog signal (green), dead time corrected photon counting signal (black) and glued signal (red). Recorded on 2014/03/05, 12:01 pm. (b) Bin shifted, range corrected analog signal (green), dead time corrected photon counting signal (black) and glued signal. Recorded on 2014/02/27, 14:49 pm . At* 1900 *m altitude an aerosol layer can be seen.*

Figure 9(b) shows a glued data set for a dizzy day with varied gluing parameters. Data were measured on 2014/02/27 between 14:49 pm and 15:48 pm and is depicted for 14:49 pm. The linear regression coefficients are $a = 69.2$ and $b = 1.4$. At 1959 m an aerosol cloud can be seen from all three signals. For special meteorological events, e.g. saharan dust intrusions, an optimized data-gluing method can be applied, which seeks not only for best fitting regression coefficients, but also for an optimized gluing region. For those events the total gluing region may stretch up to 1.5 km [Lange et al.,

2011]. Since those special events have not been recorded in this master thesis, a further application of this optimized procedure is not presented here.

3.2 Ceilometer

The ceilometer CHM15kx, see figure 10, provided by Jenoptik is an instrument mainly used for cloud height determination and vertical visibility up to altitudes of 15 km [Jenoptik, 2013]. Its measurement principle is LIDAR as described in section 2.2. Short light pulses are emitted vertically into the atmosphere where they are scattered by aerosols and molecules. The time of flight and the intensity of the backscattered light are analyzed. From this data the height assignment of the aerosol cloud layers and the visibility are determined. As for the LIDAR system, it is aimed in this thesis to additionally derive information about atmospheric parameters like the backscatter and extinction coefficients from the raw backscatter signal.

3.2.1 Components

The ceilometer, as can be seen in figure 10, is located at the Plataforma Solar de Almería in about 5 m distance south to the LIDAR system. The corrosion resistant aluminum shell protects the modular devices, such as the laser, the telescope and the acquisition and processing system, from soiling weather impacts. The ceilometer system is oriented vertically towards the zenital direction. At the top of the instrument a low reflection window for exit and entry of the laser light is installed with a Brewster inclination angle to ensure small laser light losses and support self-cleaning [Jenoptik, 2013].

The ceilometer provides the cloud base height, up to three simultaneous layers. Like the LIDAR system, it suffers from the overlap effect, that is internally corrected with a correction function. The laser (Nd:YAG-laser, class M1) emits light pulses of 1 ns duration and 8 μJ energy of the wavelength 1064 nm. After the beam passed through the beam steering and expanding optics, the beam diameter is 90 mm with a divergence

Figure 10: *Ceilometer located at the Plataforma Solar de Almería.*

of 100 μrad. The measurement time, meaning the period of time over which the backscatter signal is averaged, is 15 s with a sample frequency of 5 - 7 kHz [Jenoptik, 2013]. The raw data is stored in a NetCDF-format.

3.2.2 Data Collection

Data collection with the ceilometer functions fully automatically. A standard measurement cycle contains the testing of the data and the evaluation of the status parameters, such as the temperature and the voltage after each measurement. If the parameter values exceed the tolerance region or a hardware error exists, a reinitialization is performed, controlled by the APD controller. Also, in case of malfunction or the absence of communication between the modules a new measuring cycle is triggered [Jenoptik, 2013]. The laser pulse energy is essentially determined by the pulse repetition rate. A decrease in pulse energy leads to an automatic decrease in pulse repetition rate. When the pulse energy falls below 4.5 kHz, an error message is issued [Jenoptik, 2013]. Error messages are sent to the user, when the window is contaminated. An automatic analysis of the reflection at the window provides information about the soiling. For signal recording, a sensitive photon counter is used, which allows the detection of low count rates, but also of noise signals. The noise performance of the receiver depends on the voltage supply [Jenoptik, 2013]. Data storage and measurement work simultaneously. The system runs day and night continuously since April 2014 at the PSA, saving the data on a daily basis in NetCDF-format.

3.2.3 Data Processing

For comparison of ceilometer data with lidar data or sun photometer data specific conditions must be valid. Because of malfunction or contaminated windows that demand a shutdown for cleaning, there are gaps in the ceilometer data, that need to be sorted out manually with a MATLAB routine. In principal, a sampling rate of 15 s serves as reference for data exclusion. Only measurements that include consecutive sampling for more than 2 min are used. Time stamps that refer to night measurements from 9 pm to 6 am are excluded from data analysis, because the sun photometer and LIDAR measure almost only during daytime.

Cloud Exclusion For comparison with sun photometer data it is essential to differentiate between measurements performed at cloud-free time periods or at cloudy conditions. As further discussed in section 3.3.2, the sun photometer data is processed by AERONET and gives results for time periods where a clear atmosphere was given. The ceilometer measures up to three cloud base heights that data are also saved in the NetCDF-file. Therefore, only data that indicates a cloud-free atmosphere, meaning that no cloud base height is given, is used for comparison with the sun photometer.

Downsampling For the selected periods, the ceilometer data must be downsampled. This means that the sampling rate of 15 s must be downsampled manually to 1 min to match the LIDAR and sun photometer sampling rates. Thus, the backscatter signal of the ceilometer is averaged over the respective time interval of one minute. This time interval also coincides with the temporal resolution of the temperature and pressure profiles that are acquired at the PSA and that have an impact on the derivations of

the backscatter and extinction coefficients using the Klett-Fernald method, see section 2.5.

3.3 Sun Photometer

The multiband sun photometer CE318 provided by Cimel is an instrument for measuring optical properties of the atmosphere, providing information about the quantity and optical character of aerosols. It measures the direct solar irradiation of the wavelengths: 340, 380, 440, 500, 675, 870, 1020 and 1640 nm. On the basis of reference values and the current intensity of the sun's radiation, optical properties of the atmosphere can be deduced. The sun photometer is connected to the AERONET (Aerosol Robotic Network), which is a federation of ground based remote sensing aerosol networks. It provides a long-term, continuous and readily accessible database of aerosol optical properties [AERONET, 2014]. The instrument is located at the PSA, Tabernas, Spain, in about 2 m distance to the LIDAR system and the ceilometer.

3.3.1 Components

The sun photometer, depicted in figure 11 is a portable instrument that consists of three parts: an electronic box, a two axis motorized system and a sensor head [Cimel, 2001]. The electronic box is the control and measuring unit and contains the CPU card, which is the central processor of the instrument. It connects the sensors for the sun's luminance and controls the motorized tracking system that carries the optical head, which can rotate around the vertical and horizontal axis [Cimel, 2001]. Two detectors, installed at the sensor head, measure the direct sunlight over a range of particular wavelengths. The selection of wavelength is achieved with the motorized filter holder by eight attached narrow filters in front of the detectors.

Figure 11: *Sun photometer located at the PSA, Spain.*

3.3.2 Data Collection

Since the sun photometer is an autonomously operating instrument, the data collection functions fully automatically. Data processing and analysis is performed by AERONET with the AERONET standard cloud-screening algorithm and the AERONET inversion code [Smirnov et al., 2000, Holben et al., 1998]. The code inverts sky radiances simultaneously at all measured spectral channels. Aerosol particles are assumed to be either spherical or non-spherical and the atmosphere is assumed to be plane-parallel [Cimel, 2001]. The retrieval method provides inter alia the aerosol optical depth for the given channels. It is differentiated between three levels of classification. Level 1.0 refers to the AOD of uncorrected data, Level 1.5 refers to a cloud correction, where high AODs that indicate clouds are extracted from the data. Level 2.0 then corresponds to a cloud corrected and quality assured retrieval method, that sets the limits for uncertainties lower and thus yields a reduced number of data points due to data removal. The processed data files are freely accessible via the AERONET website [AERONET, 2014].

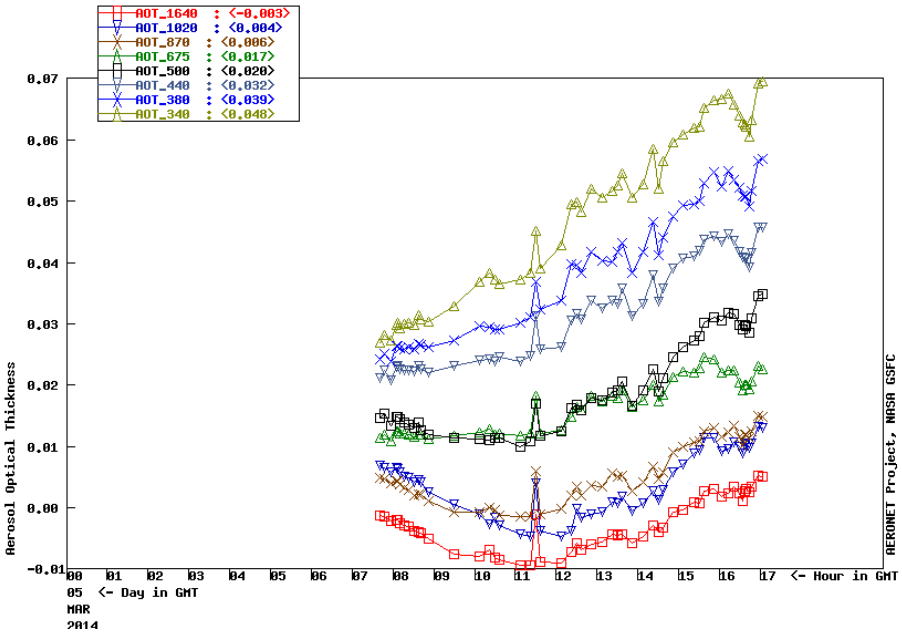

Figure 12: *The AODs for 8 wavelengths plotted over time. Recorded on 2014/03/05.*

In figure 12 an exemplary data file is depicted. The aerosol optical depth is plotted over the time axis for the eight available wavelengths. Data were acquired on the 2014/03/05 between 7:30 am and 5 pm at the PSA, when the atmosphere was clear, containing no visible clouds. High wavelengths are less scattered by particles or molecules resulting in smaller backscatter and extinction coefficients. Therefore, high wavelengths yield to lower values for the AOD than low wavelengths.

With the obtained AODs at 340, 500, and 1020 nm, the Ångström parameters have been calculated using the modified Ångström approach [Bird and Riordan, 1984, Gueymard, 2001]. This approach allows to determine the AODs for the specific wavelengths 355, 532 and 1064 nm from the measured AODs of the sun photometer channels. The simplified methodology considers two different spectral regions, above and below the threshold wavelength $\lambda_0 = 500\,\text{nm}$. The Ångström coefficients A_i and B_i are determined

with:

$$AOD = B_i \left(\frac{\lambda}{\lambda_1} \right)^{A_i}, \tag{49}$$

where λ is the variable wavelength and $\lambda_1 = 1000\,\text{nm}$ is the reference wavelength [Gueymard, 2001]. If $\lambda < \lambda_0$, $A_i = A_1$, otherwise, $A_i = A_2$. Further, $B_i = B_1 = 2^{A_2 - A_1} B$ if $\lambda < \lambda_0$ and $B_i = B_2 = B$ otherwise. With the according Ångström coefficients the AODs for the specific wavelengths of 355, 532 and 1064 nm, that correspond to the operating channels for LIDAR and ceilometer measurements are retrieved.

4 Results

In this section the aerosol extinction coefficient is derived from data acquired with the LIDAR and ceilometer system using the Klett-Fernald method. The impact of the reference height, the lidar ratio and the background correction to the method are discussed. Furthermore, the AODs determined with the sun photometer, the LIDAR and the ceilometer are intercompared, using the sun photometer AODs as reference values. The overlap correction functions presented in section 2.7 are determined and applied to the LIDAR backscatter signal. Then again, the corrected LIDAR data is compared to the sun photometer data. Finally, the extinction coefficient determined with the LIDAR is compared to scattermeter data.

4.1 Determination of the Aerosol Extinction Coefficient

To derive the aerosol extinction coefficient with the Klett-Fernald method as described in section 2.5, the reference height r_{ref} and the lidar ratio LR need to be specified. LIDAR data analysis is performed using MATLAB. The raw signal from photon counting and analog is glued together as described in section 3.1.5 and background corrected. For temperature and pressure determination on-site measurements have been performed, giving the ground values T_g and p_g with a temporal resolution of one minute. Commonly known standard profiles released by the *Air Force Geophysics Laboratory* in 1986 are used for scaling the temperature and pressure profiles to the ground values [Anderson et al., 1986]. The *afglms*-atmospherical profile for midlatitude summer has been applied to the ground values with an according output spatial resolution of 7.5 m.

The refractive index n_s and the depolarization factor δ are given by Raymetrics:

$$n_s^2 - 1 = \begin{cases} 5.7148 \cdot 10^{-4} & 355\ nm \\ 5.5647 \cdot 10^{-4} & 532\ nm \\ 5.48 \cdot 10^{-4} & 1064\ nm \end{cases} \qquad \delta = \begin{cases} 0.0301 & 355\ nm \\ 0.0284 & 532\ nm \\ 0.0273 & 1064\ nm \end{cases} .$$

The number density of molecules at standard air conditions N_{S0} is $2.547 \cdot 10^{25}\ \frac{\text{molecules}}{\text{m}^3}$ [Kovalev, 2004]. With these values and the additional presumptions about the reference height and the lidar ratio, the molecular backscatter and extinction coefficients can be calculated and furthermore the aerosol backscatter and extinction coefficients can be determined.

4.1.1 Sensitivity - Reference Height

The specific choice of a reference height is an important factor for the determination of the atmospheric parameters, as the Klett method is very sensitive. For that reason sensitivity studies for the uncorrected lidar signals have been carried out. With the presumed lidar ratios of 58 sr and 55 sr for the 355 nm and 532 nm wavelengths, respectively, the reference height r_{ref} has been varied for sensitivity studies. Figure 13 shows the aerosol extinction coefficient for five different reference heights varying from $r_{ref} = 2000$ m to $r_{ref} = 7000$ m plotted over the range from 0 - 5000 m. The data were acquired on the 2014/03/05, 11:47 am with the LIDAR system.

The coefficient is derived for both wavelengths, 355 nm in figure 13(a) and 532 nm in figure 13(b). The results reveal that there is no proportional dependency between

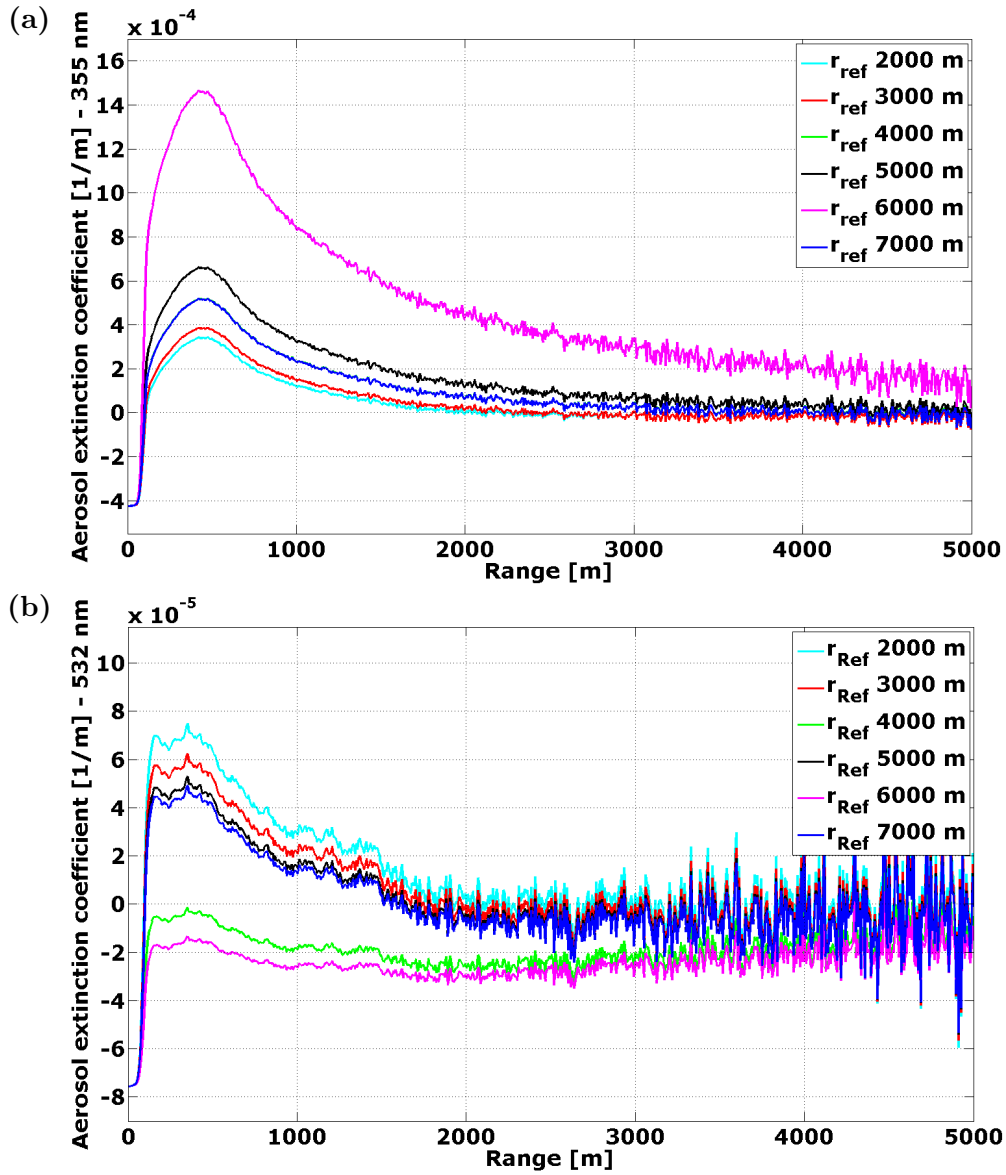

Figure 13: *Aerosol extinction coefficient with varying reference height for (a) 355 nm with LR = 58 sr and (b) 532 nm with LR = 55 sr. Recorded on 2014/03/05, 11:47 am.*

r_{ref} and α_{aer}, in fact, the reference height meets singularity conditions in the Klett-Fernald method. As can be seen in figure 13(a), an increase in the reference height from 2000 m to 6000 m leads to an increase of the aerosol extinction coefficient for the 355 nm wavelength. When assuming a reference height of 7000 m the aerosol extinction coefficient reveals a similar result as for the 4000 m reference height. Figure 13(b) shows that the aerosol extinction coefficient for the 532 nm wavelength is smaller than 0 over the complete range, when assuming a reference height of 4000 m and 6000 m.

Negative values for the aerosol extinction coefficient are due to the SNR in high ranges of lidar sounding. The backscatter signal reveals negative values after background correction and therefore leads to a negative aerosol extinction coefficient. To avoid negative values in the backscatter signal at the reference height, the reference height should be set low. According to [Mattis et al., 2008] the reference height lies between 5 - 7 km. Hence, a reference height of 5000 m was chosen for the following considerations.

4.1.2 Sensitivity - Lidar Ratio

To analyze the sensitivity of the Klett-Fernald method regarding the lidar ratios, the reference height r_{ref} was kept constant and the lidar ratios have been varied. Figure 14 shows the aerosol extinction coefficient α_{aer} for 355 nm and 532 nm with the lidar ratios ranging from 20 sr to 70 sr. α_{aer} exhibits a proportional dependency to the variation of LR for both wavelengths. An increase of the LR leads to an increase of the aerosol extinction coefficient for both wavelengths. It can be seen that a variation of LR from 20 sr to 70 sr results in an increase of the aerosol extinction coefficient by almost one magnitude.

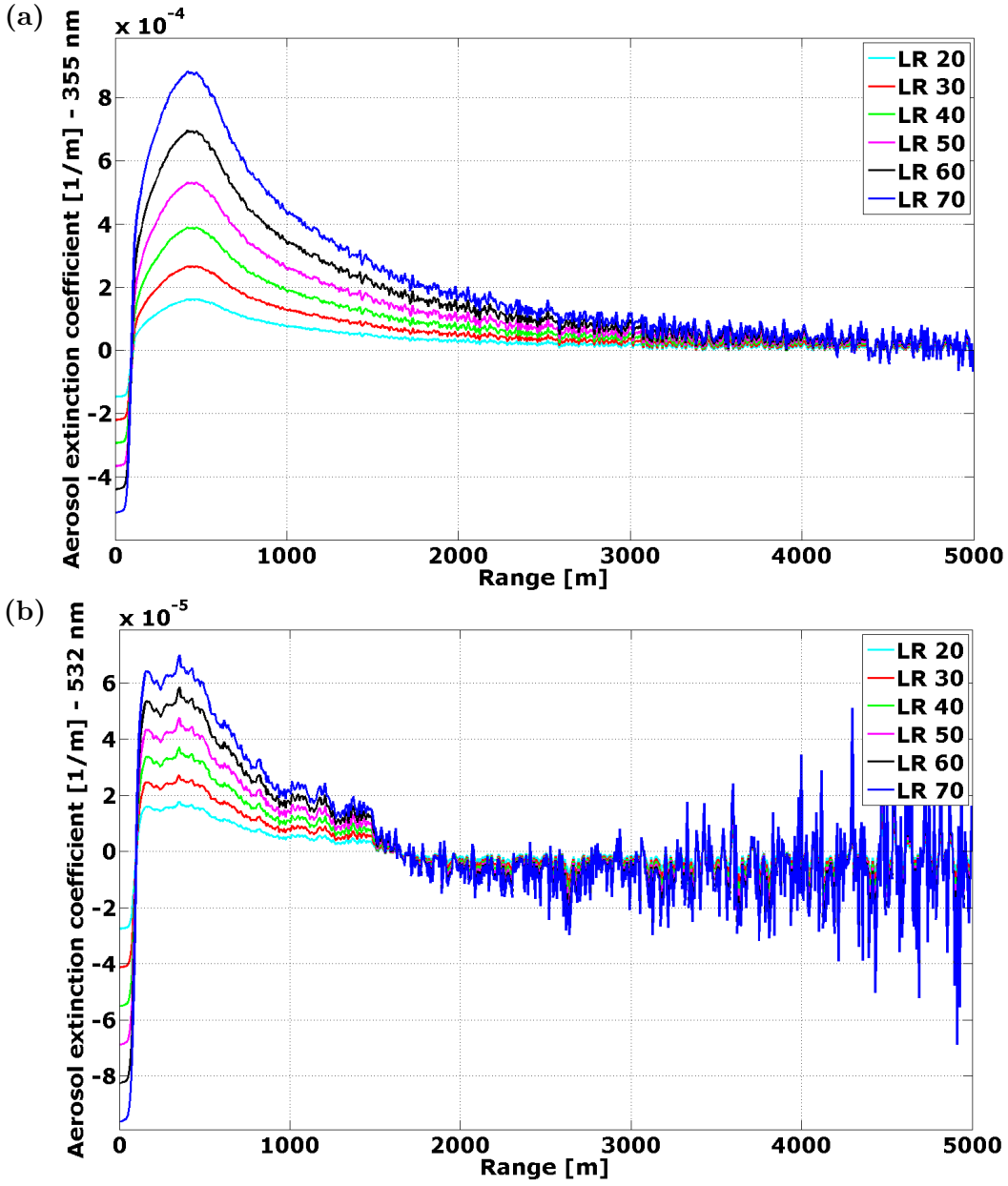

Figure 14: *Aerosol extinction coefficient with varying lidar ratio for (a) 355 nm and (b) 532 nm with reference height = 5000 m. Recorded on 2014/03/05, 11:47 am.*

From the elastic backscatter signal of the LIDAR system no information about the size of aerosol particles and thus the lidar ratio can be derived. Therefore, the values for the lidar ratio are taken from literature, see section 2.5.2. For the ongoing studies the lidar ratios of 58 sr for 355 nm and 55 sr for 532 nm were chosen.

4.1.3 Background Correction

Background radiation is a source of error during LIDAR measurements. Diffuse sunlight reaches the telescope and leads to a randomly change of signal for the LIDAR channels. Generally, the signal-to-noise ratio for shorter wavelengths is better than for

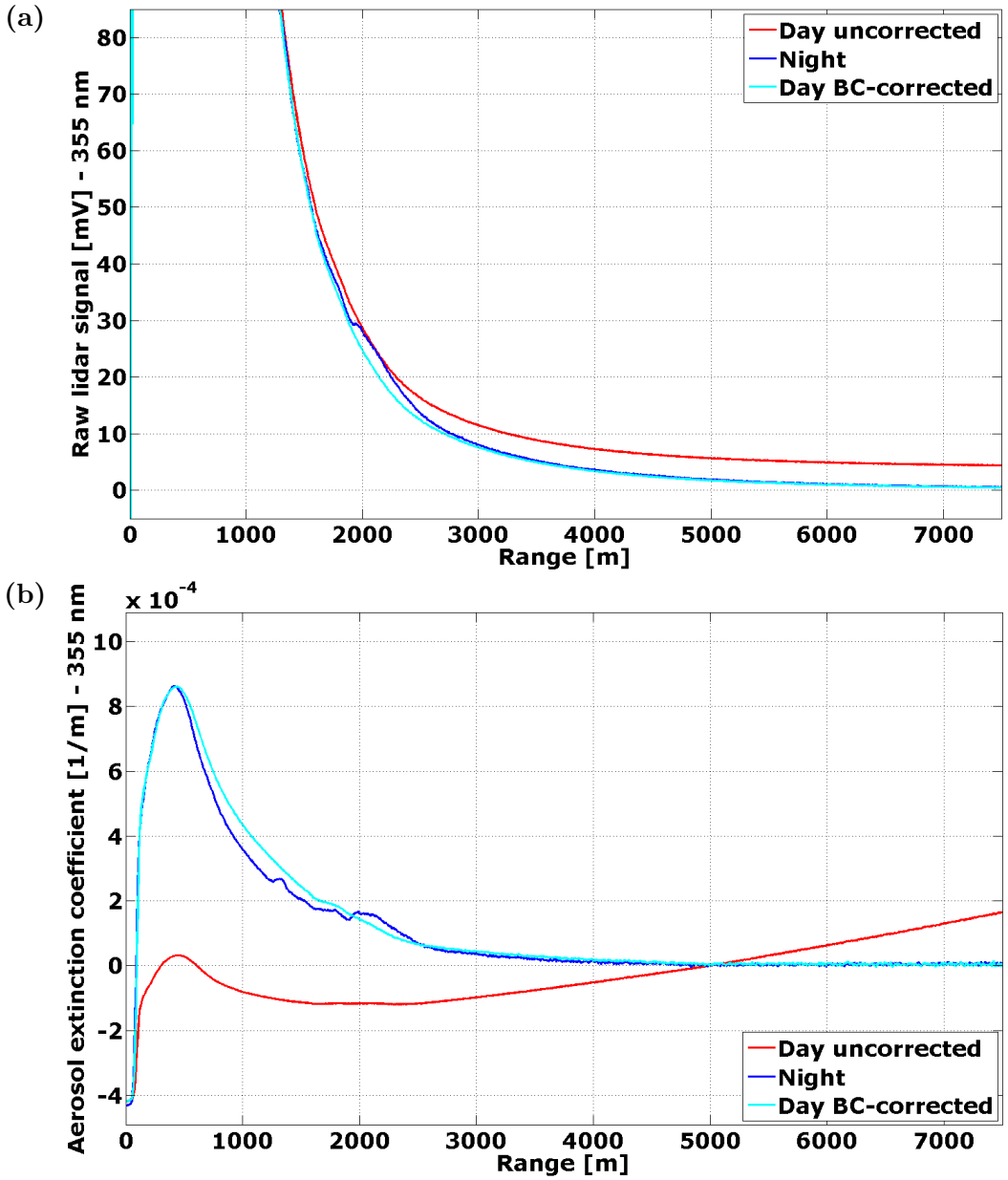

Figure 15: *(a) Raw lidar signal and (b) aerosol extinction coefficient for 355 nm, derived from the uncorrected signal (red), the background corrected signal (cyan) and the signal from night measurement (blue). Recorded on 2014/03/17, 14:13-18:07 pm and 19:03-19:46 pm.*

higher wavelengths, as can be seen in the figures 13 and 14. Since a night measurement has been performed on the 2014/03/17, see figure 16, the background corrected signals can be compared to night measurement signals to check if a background correction is of importance for the derivation of the extinction coefficient. The results for the background correction for the 355 nm wavelength are depicted in figure 15. The data were acquired during day time at 14:13-18:07 pm and at night time at 19:03-19:46 pm. The signals and aerosol extinction coefficients are depicted over a range from 0 to 7500 m and have been averaged over the respective time periods. In addition to the uncorrected day and night measurement signals, the background corrected signal from day measurement is shown in figure 15(a).

The recorded backscatter signal of the day measurement contains background signals. From the data of the night measurement can be seen that the background radiation has an impact on the signal for the region above 1000 m. Figure 15(b) shows the aerosol extinction coefficient.

For background correction, the mean signal value of the last 50 data points (bins) of the complete range (0 - 15000 m), is subtracted from the signal. 50 bins correspond to 375 m. After background correction the signals of night and day measurements exhibit a similar behavior.

An exemplary application of the Klett-Fernald method to the uncorrected signal from the day measurement yields to a strong deviation of α_{aer} between the corresponding day and night results, see 15(b)(red). After background correction the profiles for the aerosol extinction coeffient exhibit a similar behavior. Small deviations are due to the different atmospheric conditions during day and night performance. For further considerations a background correction has been applied to the raw backscatter lidar signals.

Figure 16: *METAS, PSA on the 2014/03/17, 19:40 pm during LIDAR measurements.*

4.2 Intercomparison of Sensors

The data of the LIDAR, the ceilometer and the sun photometer can be intercompared when representing the AOD. For the LIDAR and the ceilometer, the calculation of the AOD was accomplished using the Klett-Fernald method and integrating over the aerosol extinction coefficient up to the reference height of 5000 m according to equation 1. The determination of the AOD with sun photometer data was performed as described in section 3.3.2.

4.2.1 LIDAR - AERONET

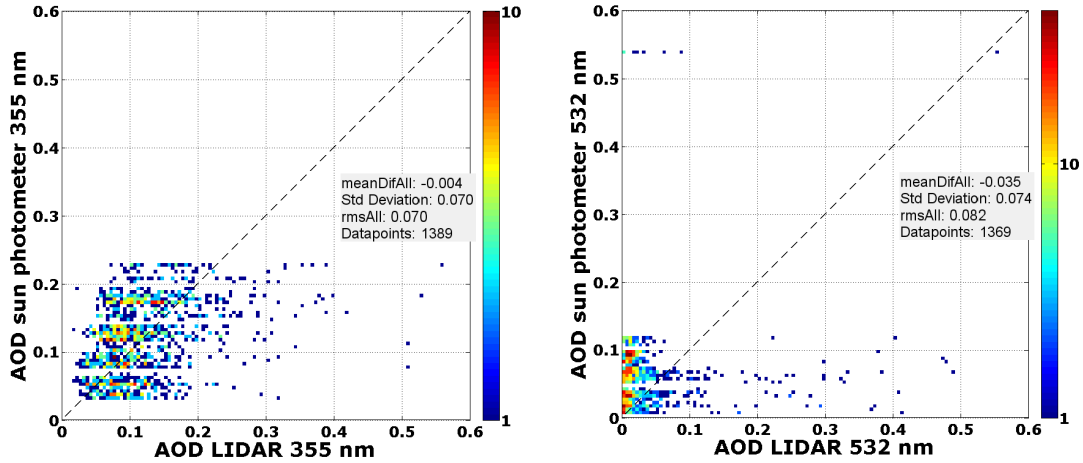

Figure 17: *AODs of sun photometer and LIDAR for 355 nm (a) and for 532 nm (b).*

To compare LIDAR and sun photometer AODs, adequate time periods need to be chosen with the presumption that the atmosphere is completely cloud-free. This presumption is necessary for the data processing of AERONET. In other cases, i.e. a cloudy atmosphere, the level 1.5 algorithm will lead to gaps in the data set. For the purpose of cloud exclusion the continuously measuring ceilometer is taken as a reference, as earlier described in section 3.2.3.

It is expected that the AODs determined with the LIDAR system lie below the values obtained with the sun photometer due to the overlap problem of the LIDAR.

As a fast and simple correction method for the overlap problem of the LIDAR, the measured signal was held constant for the region of incomplete overlap with the value corresponding to 120 m. The results are unchanged from the results with no signal correction and presented in figure 17. Keeping the signal constant for the lowest range bins is an insignificant correction method that is furthermore reduced by the range correction implied in the Klett-Fernald method. More promising correction methods are applied and the results are presented in section 4.3.

For analysis and comparison data recorded between the 2014/03/04 and 2014/03/20 has been used, leading to a total number of 1399 data points. One data point refers to an average of one minute measurement for the LIDAR. For the calculation of the AOD from the aerosol extinction coefficient, only positive values were used.

The AODs of the sun photometer and LIDAR are plotted in figure 17(a) for the 355 nm wavelength and in 17(b) for the 532 nm wavelength. To keep errors comparable for both wavelengths, all outliers above an AOD of 0.6 are sorted out before error analysis. Also values of the AOD indicating 0 are removed from the data, causing a variation in the number of data points as depicted in figure 17(a) and 17(b). For the 355 nm wavelength 1389 data points and for the 532 nm wavelength 1369 data points have been used for analysis. The color bar is set to a logarithmic scale for better distinction of multiple occupation of the same coordinate point. The diagonal line indicates the region where LIDAR AODs and sun photometer AODs would coincide. A factor for scattering around this line is the inhomogeneity of the atmosphere, since both instruments do not measure the exact same sample of air column.

The expectation of lower AODs for lower wavelengths is experimentally verified. For the 355 nm wavelengths the data accumulation exhibits a linear behavior, meaning that for increasing AODs measured with the LIDAR, the corresponding AODs of the sun photometer are also increasing. The majority of values lies between 0.03 and 0.25. The mean difference (MD) between the AOD of the LIDAR and reference AOD of the sun photometer is -0.004 with $mean(AOD_{LIDAR}) < mean(AOD_{AERONET})$. The standard deviation (STD) as a measure of the amount of variation from the average is 0.070 and the root mean square (RMS), as a measure of the magnitude of the varying values, is also 0.070. The errors are calculated with the sun photometer AODs as reference data for the LIDAR AODs. From the scatter plot can be seen, that the processed AERONET data exhibits constant AODs for longer time periods, whereas the LIDAR data fluctuates, due to the sensitive retrieval algorithm. The absolute errors for the AOD retrieval with the Cimel sun photometer vary between 0.01 and 0.02 [Holben et al., 1998].

A source of error for the LIDAR data processing is the varying lidar ratio. The ratio is held constant over altitude and time, although the physical understanding of the lidar ratio demands an atmosphere dependent determination for each altitude and time. Analogous, the AODs of the sun photometer and the LIDAR for the 532 nm wavelength are depicted in figure 17(b). From the plot can be seen, that the LIDAR AODs are smaller than the sun photometer AODs. The sun photometer AODs vary from 0.01 to 0.13, whereas the LIDAR AODs accumulate around 0.02. Also from the mean difference of -0.035 can be seen, that the LIDAR data exhibits a smaller mean AOD than the sun photometer data. The standard deviation of 0.074 and the root mean square of 0.082 are higher than the errors of the 355 nm results, showing that the scattering of the LIDAR data around the reference data of the sun photometer is stronger for the 532 nm wavelength, although the mean AODs of this wavelength are lower than for the 355 nm wavelength. Another factor that impacts the 532 nm channel stronger than the 355 nm channel is the background noise at the reference height of 5000 m. For 532 nm, the range corrected signal includes negative values after the background correction. Those values lead to a negative extinction coefficient at some ranges and can therefore not be considered when calculating the AOD. Accordingly, the AOD for the LIDAR 532 nm channel is expected to be lower than the reference values.

A significant source of error, besides the uncertainty of the lidar ratio, is the incomplete overlap of the receiver's and laser's fields of view. Both fields of view coincide above a range of 120 m. Below this range an incomplete signal is recorded that leads to a smaller aerosol extinction coefficient and consequently a lower AOD.

4.2.2 LIDAR - Ceilometer

As results of the comparison between LIDAR and ceilometer a difference in AODs is expected, caused by the difference in detection wavelengths, since the AOD is wavelength dependent and decreases with increasing wavelengths. Nevertheless, a temporal change in atmospheric conditions must be detected by both instruments.

The ceilometer aerosol extinction coefficient is calculated with the Klett-Fernald method, analogous to LIDAR calculations. The time resolution is downsampled to one minute time steps. The lidar ratio for the 1064 nm wavelength is approximated to be 45 sr and the reference height is 5000 m. Temperature and pressure profiles have been determined using the ground values at the PSA and scaling the standard profiles [Anderson et al., 1986]. An exemplary aerosol extinction coefficient profile is shown in figure 18. Data is recorded on the 2014/03/05 at 12:58 pm and 13:44 pm. The aerosol extinction coefficient determined with the ceilometer for the 1064 nm is expected to be generally smaller than for the LIDAR 355 nm and 532 nm channels.

The aerosol extinction coefficient for the 1064 nm wavelength results in negative values due to the retrieval method for measurements performed when the atmosphere was very clear, see figure 18. The integration of a negative aerosol extinction coefficient leads to negative values for the AOD, accordingly. When compared to figure 12, smaller values for the AOD at high wavelengths at the 2014/03/05 is in accordance with the sun photometer data. The AERONET 1.5 level retrieval method allows negative values for AODs down to −0.1 [AERONET, 2014]. For the purpose of comparison also with LIDAR measurements, negative values of the AOD are omitted. Data measured between the 2014/03/03 and 2014/03/20 has been used. The AODs determined with ceilometer measurements are plotted together with the AODs determined with the LIDAR system for 355 nm 19(a) and for 532 nm 19(b) and the ceilometer functions as

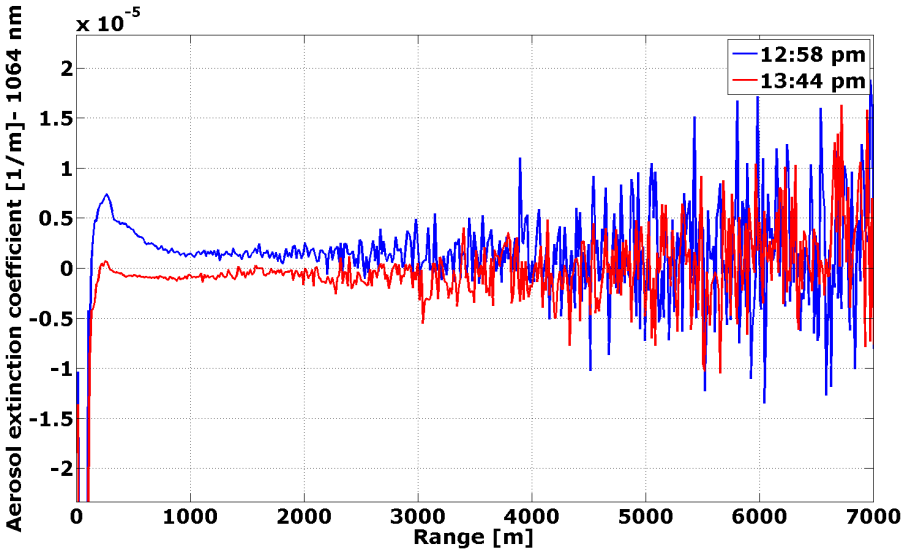

Figure 18: *Exemplary aerosol extinction coefficient measured with the ceilometer at 1064 nm on 2014/03/05 at 12:58 pm (blue) and at 13:44 pm (red).*

a reference for the LIDAR. After cloud exclusion a data set consisting of 1547 data points was found. For error calculations all values equal or smaller than 0 and greater than 0.6 are excluded and subsequently the number of data points decreased to 1463

and 1404 for 355 nm and 532 nm, respectively. This decrease is due to the fact, that a negative aerosol extinction coefficient leads to a negative AOD and therefore is excluded from the data.

In figures 19(a) and 19(b) can be seen, that the ceilometer AODs compared to the LIDAR AODs for the 532 nm channel lead to a smaller mean difference than for the 355 nm channel. This was an expected behavior, because the AOD is wavelength dependent. The STD and the RMS of the comparison with ceilometer AODs to LIDAR AODs for the 355 nm are smaller than for the 532 nm channel. A reason for this is found in the higher SNR for the 532 nm wavelength. At the reference height the range corrected 532 nm lidar signal exhibits strong irregularities causing a greater scattering of AODs than for 355 nm.

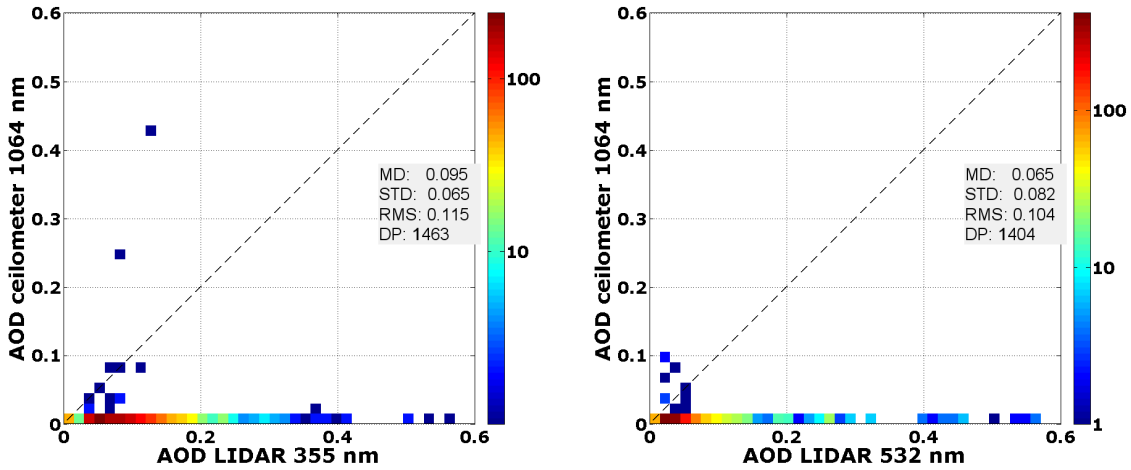

(a) (b)

Figure 19: *AODs of ceilometer and LIDAR for 355 nm (a) and for 532 nm (b) with cloud-free atmosphere.*

In figure 20, all data are shown without any specific cloud exclusion, so that also data of days with hazy atmospheric conditions were analyzed and AODs also greater than 0.6 are plotted. The total number of data points is 2210 and all AOD values, equal or smaller than 0 and greater than 1, are sorted out for error calculations. The MD, STD and RMS for the 355 nm channel are significantly bigger than for the cloud-free data set. This is also due to the higher range of AODs. For hazy days the AODs tend to be greater than 0.6, causing a larger error scale. Particularly noticeable from the figure 20(b) is the scale change in the color bar. The dark red pixel close to the coordinate origin indicates that more than thousand data points are scattered around this sample pixel. The errors for the 532 nm channel are small, because most part of the AOD data is close to 0 for LIDAR and ceilometer.

From both figures 19 and 20 can be seen that the AODs acquired with the ceilometer are significantly smaller than for the LIDAR. The errors of the AODs obtained with the 532 nm wavelengths compared to the ceilometer data is smaller than for the 355 nm wavelength, because the AOD is wavelength dependent and the 532 nm wavelength consequently leads to smaller values of AOD for this channel. The data acquired with

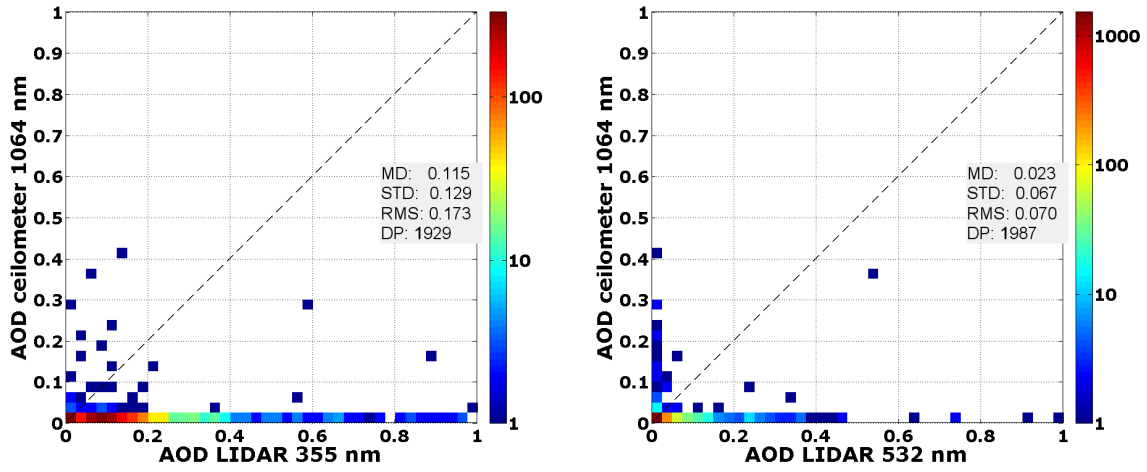

(a) (b)

Figure 20: *AODs of ceilometer and LIDAR for 355 nm (a) and for 532 nm (b).*

hazy atmospheric conditions show greater errors than for clear atmospheric conditions. A source of error for the ceilometer is the instability in signal at the reference height. It is also possible that higher cloud layers were detected with the LIDAR system, but not with the ceilometer, resulting in bigger errors than if only clear conditions were assumed. For that reason, it is necessary to compare also the sun photometer AODs with the ceilometer AODs.

4.2.3 Ceilometer - AERONET

For the comparison of the sun photometer AODs to the ceilometer AODs a great data set, acquired between the 2013/11/07 and 2014/06/24 has been analyzed. The AODs of both instruments are expected to show the same values and scatter close to the indicated diagonal in the scatter plot.

Again, the cloud exclusion routine narrowed the data set down to a total number of 44 260 data points, where one data point corresponds to one minute averages of sampling. After sorting out all points equal to 0 and greater than 0.6 before error calculation, the number of data points has been reduced to 38 981. For the determination of the AOD from the ceilometer signals at 1064 nm, a lidar ratio of 45 sr and a reference height r_{ref} of 5000 m has been assumed. The results are shown in figure 21. For the sun photometer, constant values over a larger period of time are characteristic, while the ceilometer is able to measure fluctuating changes in the atmosphere. For error calculations, the AOD of the sun photometer was taken as a reference for the ceilometer. From the AODs mean difference can be seen that the AODs acquired with the ceilometer are smaller than for the sun photometer, which was unexpected since the same wavelength is analyzed for both instruments. Around 10 000 data points coincide very close to the coordinate origin, which results in comparably small errors for the standard deviation and the root mean square. It can also be seen, that although the ceilometer data indicated an aerosol free atmosphere with the cloud exclusion routine and shows AODs at 0.01, the sun photometer measured values greater than 0.5. This

suggests that a ceilometer calibration must be performed. A misalignment could cause an exit of the laser beam out of the receiver's FOV before reaching the reference height at 5 km. Therefore, the backscatter signal could be reduced at higher regions, causing also a reduction in the extinction coefficient, when the *far-end* Klett method is applied.

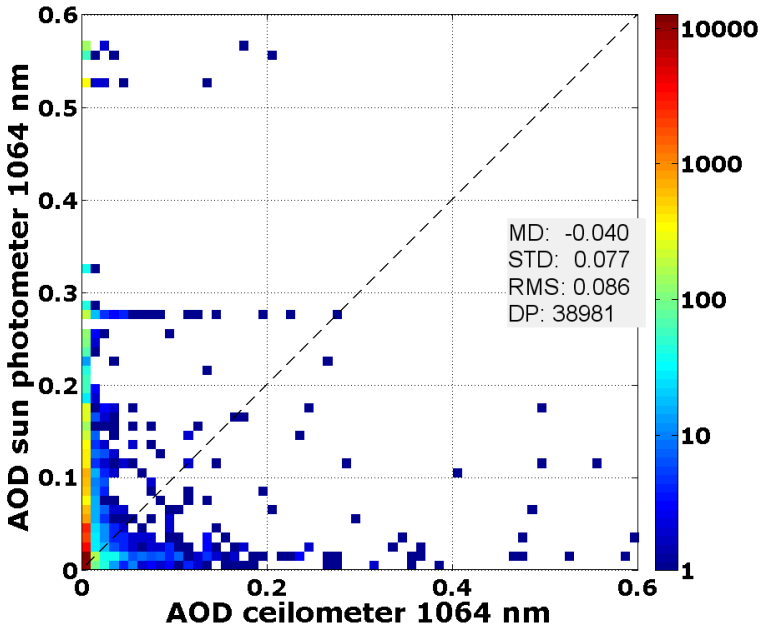

Figure 21: *AODs of sun photometer and ceilometer at 1064 nm.*

4.3 Overlap Correction of the Lidar Signal

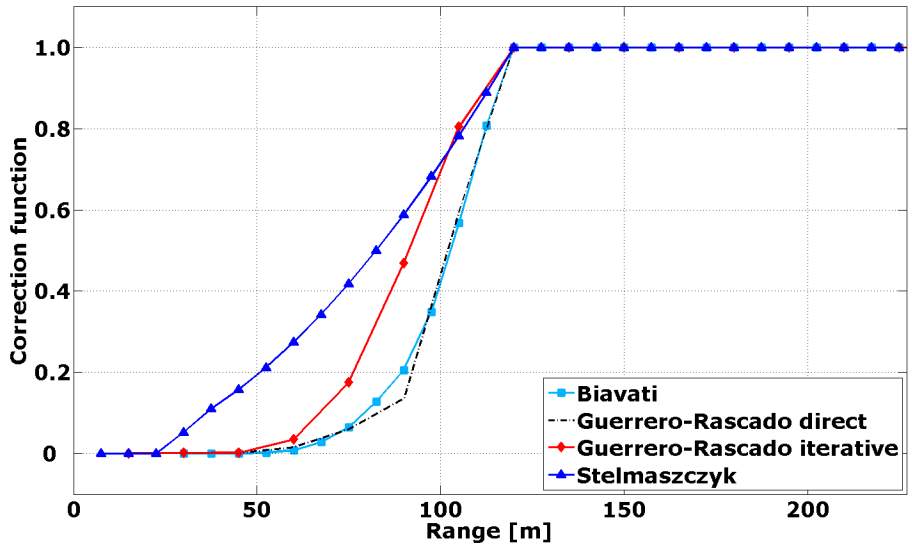

Figure 22: *Correction functions.*

The aerosol extinction is expected to be comparably high for the lowest 120 m, due to stirred-up dust and urban pollution. Presuming a higher aerosol density, the laser light is scattered stronger by particles in this region. Hence, the backscatter signal in the lowest region is also expected to reach its maximum values, assuming a cloud-free atmosphere. For the evaluation of the correction functions, the sun photometer data served as a reference for the ongoing considerations.

The three correction functions presented in section 2.7 were generated using MATLAB and are plotted in figure 22. Since the overlap problem is exclusively due to the geometrical properties of the LIDAR setup, the correction functions are wavelength independent. All correction functions are normalized to 1 in the full overlap region.

The analytical correction function, see figure 22 (dark blue), was found with the specifications stated in section 3.1.1 and the method described by Stelmaszczyk et al. (2005), see section 2.7.1. The correction function reveals values equal to 0 for the first 4 range bins, corresponding to 30 m and can therefore only correct the signal down to the first 30 m of the measurement range.

The correction function proposed by Biavati et al. (2011) was calculated from tilted measurements with an elevation angle $\omega = 20°$ and vertical measurements. Data of the 2014/03/17 beginning at 13:29 pm was used with 5 min averaging for single measurements. Optimal results could be achieved by averaging the data that was recorded vertically, before and after an elevated angle measurement was performed. 25 iterations were applied to generate the correction function, which is valid for altitudes down to 41.04 m. Below this altitude, the backscatter signal is held constant for the corresponding range bins, causing a maximum in the aerosol extinction coefficient at 45 m, as can be seen in figure 24(b).

The correction method proposed by Guerrero-Rascado et al. (2010) leads to two different correction functions for the *direct* and the *iterative* approach, indicated as black dashed line and red diamond line in figure 22. For both approaches the data recorded on the 2014/03/17 between 14:13 pm and 17:18 pm was averaged over the whole time

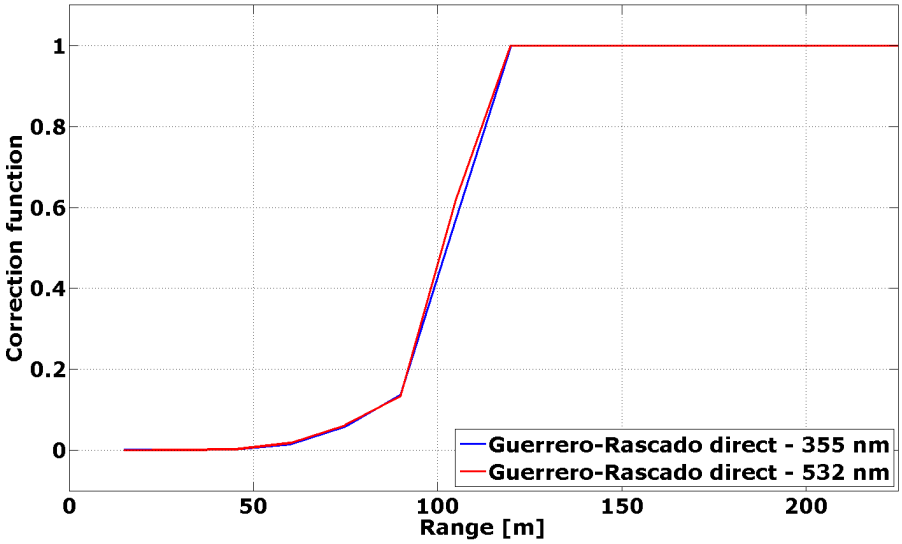

Figure 23: *Guerrero-Rascado direct correction function for 355 nm and 532 nm of averaged data. Recorded on 2014/03/17, 14:13-17:18 pm.*

period. This correction method uses the ceilometer as reference, which measures with a spatial resolution of 15 m. The correction function is consequently valid for altitudes greater than 15 m.

The correction functions by Biavati et al. (2011) and Guerrero-Rascado et al. (2010) are derived separately from the lidar backscatter signals at the 355 nm channel and at the 532 nm channel. The determined correction functions have then been averaged to achieve a wavelength independence. An exemplary plot showing the difference between the correction functions generated with the 355 nm and the 532 nm wavelength is displayed in figure 23 for the *direct* method proposed by Guerrero-Rascado et al. (2010).

The three correction functions are applied to the signal by division, as can be seen in figure 24(a). The impact on the resulting aerosol extinction coefficient is displayed in figure 24(b). For that figures, the data of the 2014/03/05, 12:34 pm is used. The greatest impact on the signal is obtained by the correction function proposed by Biavati et al. (2011), followed by the correction function proposed by Guerreo-Rascado et al. (2010). The smallest modification to the signal occurred with the correction function of Stelmasczcyk et al. (2005). These results are also reflected in the aerosol extinction coefficient.

Consequently, for the corrected aerosol extinction coefficient the most significant modification is achieved when using the correction function proposed by Biavati et al. (2011), see 24(b). For clear atmospheres, the aerosol extinction coefficient is expected to be significantly higher in the lowest hundred meters of the troposphere in comparison to higher altitudes. For that reason, the correction functions proposed by Biavati et al. (2011) and Guerreo-Rascado et al. (2010) seem best suited as a correction function for the LIDAR signal. Further evaluation of the correction functions is made in the following sections.

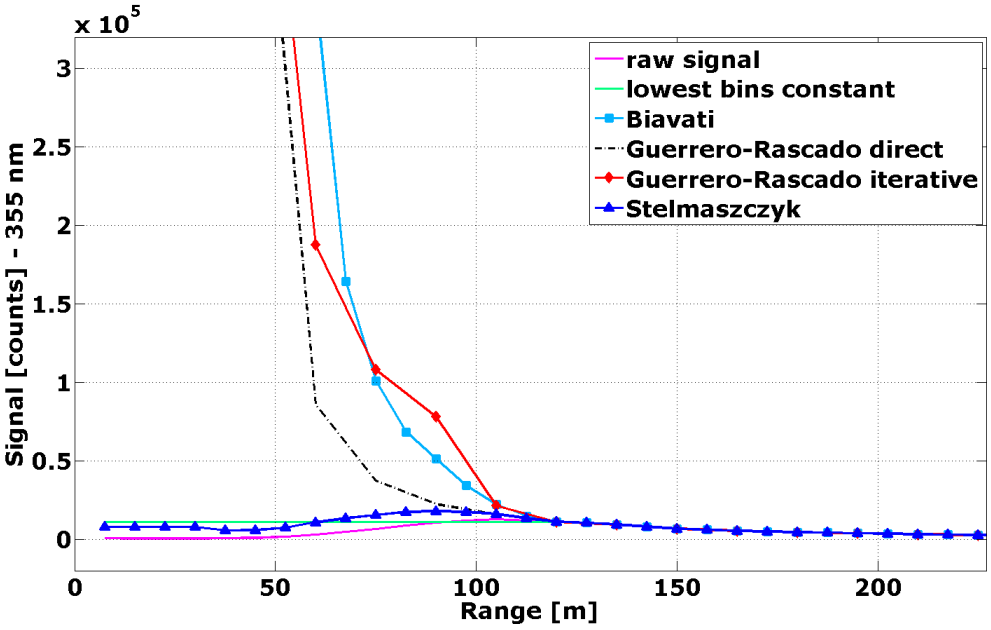

(a)

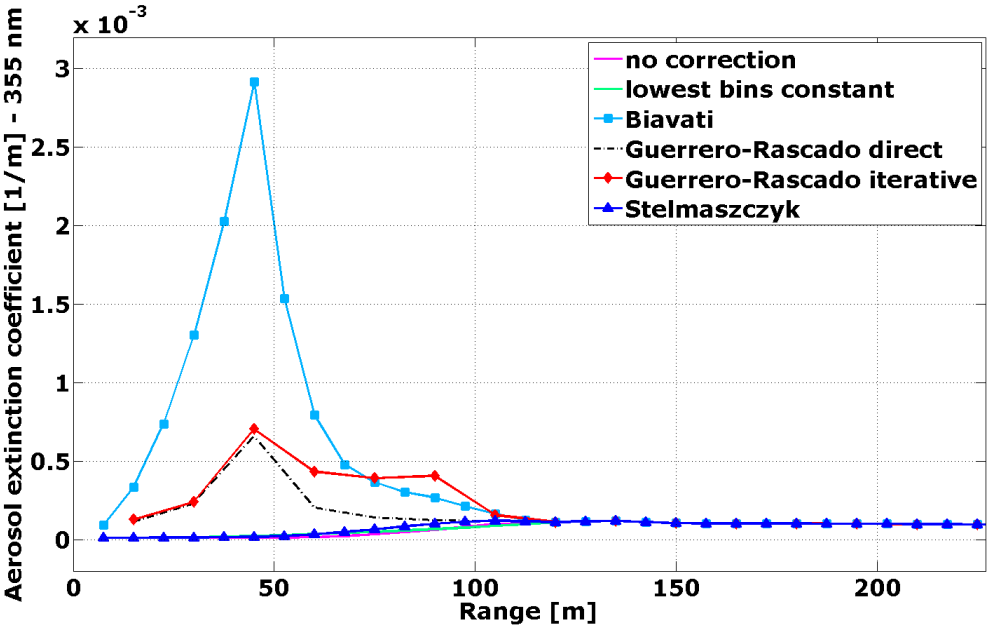

(b)

Figure 24: *Correction functions applied to the 355 nm signal (a) and the resulting aerosol extinction coefficient (b). Recorded on 2014/03/17, 12:34 pm.*

4.3.1 Stelmaszczyk

LIDAR - AERONET The correction function proposed by Stelmaszczyk et al. (2005) has a very small impact on the signal, resulting in an insignificant change in the aerosol extinction coefficient, as can be seen in figure 24(a) and 24(b). Therefore, the impact of the correction on the lidar AODs is expected to be small.

The figures 25(a) and 25(b) show the corrected AOD derived from LIDAR measurements in comparison to the AOD obtained with the sun photometer for 355 nm and 532 nm, respectively. The same data set as in section 4.2.1 is used, where uncorrected LIDAR data were compared with sun photometer data.

In comparison to the uncorrected data, the AOD of the LIDAR 355 nm channel is corrected towards the reference AODs. The mean difference, compared to the uncorrected LIDAR data is lowered to -0.002 and the standard deviation and the root mean square are lowered to 0.066. For the corrected LIDAR data, the number of data points that are unequal to 0 and smaller than 0.6 is 1385 for the corrected LIDAR data.

For the 532 nm wavelength, no change is obtained by applying the correction function by Stelmaszczyk et al. (2005). The correction functions are designed to correct the overlap problem caused by the geometrical properties of the LIDAR setup, regardless the wavelength of the measurement signal. Therefore the correction function proposed by Stelmaszczyk et al. (2005) might not suit the LIDAR system installed at the PSA.

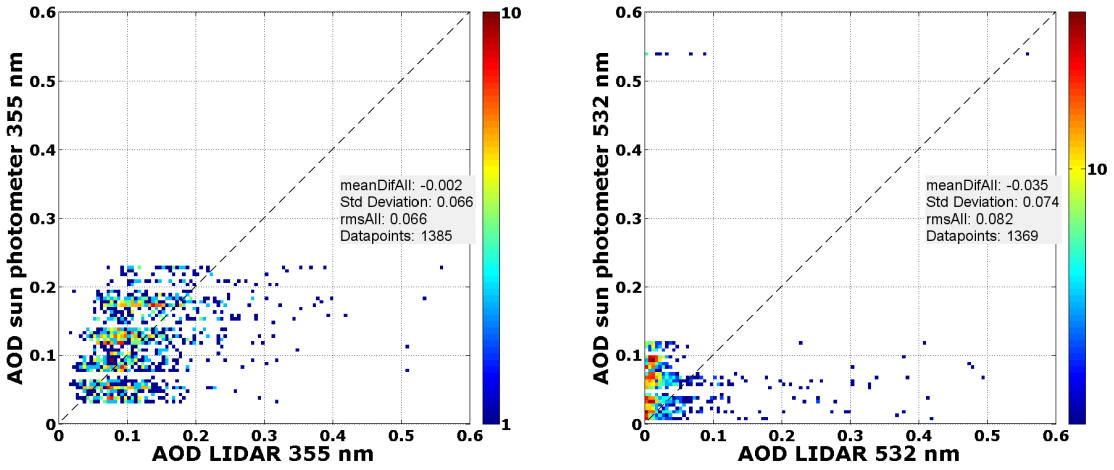

(a) (b)

Figure 25: *AODs of sun photometer and LIDAR for 355 nm (a) and for 532 nm (b) with applied correction function by Stelmaszczyk et al. (2005).*

4.3.2 Biavati

LIDAR - AERONET Since the correction function by Biavati et al. (2011) induced the greatest impact of all correction methods on the resulting aerosol extinction coefficient, the AODs obtained with the LIDAR system are expected to differ less from the reference values.

Figure 26 shows the AODs measured with the sun photometer in comparison to the AODs measured with the LIDAR system for the 355 nm and 532 nm wavelengths. For this comparison, the same data set is used previously in section2.7, when it was used for the comparison without usage of a correction function for the lidar signal. For the 355 nm signal an "over-correction" is induced by the correction function, see figure 26(a). The mean difference of AODs obtained by sun photometer and LIDAR changes from -0.004 for the uncorrected data to 0.017 for the corrected data. This is due to the fact that also outliers are corrected, leading to considerably higher values. The standard deviation and the root mean square vary insignificantly by 1 % from the values of the AOD comparison with the uncorrected data. In figure 26(b) the impact of the correction function on the 532 nm AODs is shown. The values of the LIDAR AODs increase, compared to the uncorrected data. The mean difference of sun photometer AODs and LIDAR AODs is decreased to -0.028, whereas the STD and the RMS are increased because outliers are corrected with the correction function. Also the number of data points greater than 0 and smaller than 0.6 increased to 1374 for the 533 nm wavelength, consequently causing a variation in STD and RMS. The application of the correction function by Biavati et al. (2011) leads to results, which are in good accordance with the expected effect of increasing AOD after correction.

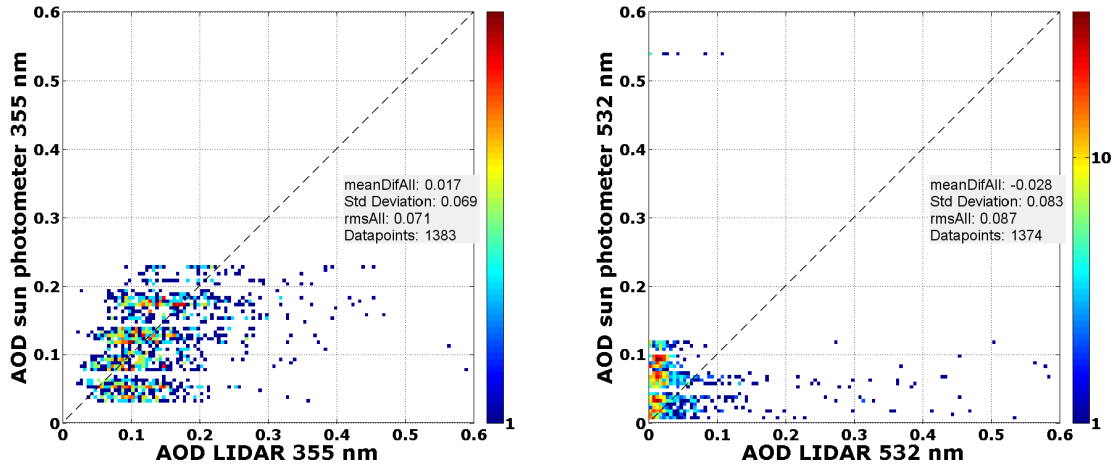

(a) (b)

Figure 26: *AODs of sun photometer and LIDAR for 355 nm (a) and for 532 nm (b) with applied correction function by Biavati et al. (2011).*

4.3.3 Guerrero-Rascado

LIDAR - AERONET Figure 27(a) and 27(b) show the AODs of the sun photometer and LIDAR, when the correction function by Guerrero-Rascado(2010) is applied to the lidar signal. The same data set has been used as for the comparison of the uncorrected LIDAR data with the sun photometer data, see section 17, has been used. As expected, the correction function obtained with the *iterative method* has a greater impact on the resulting AODs, than the correction function obtained with the *direct method*.

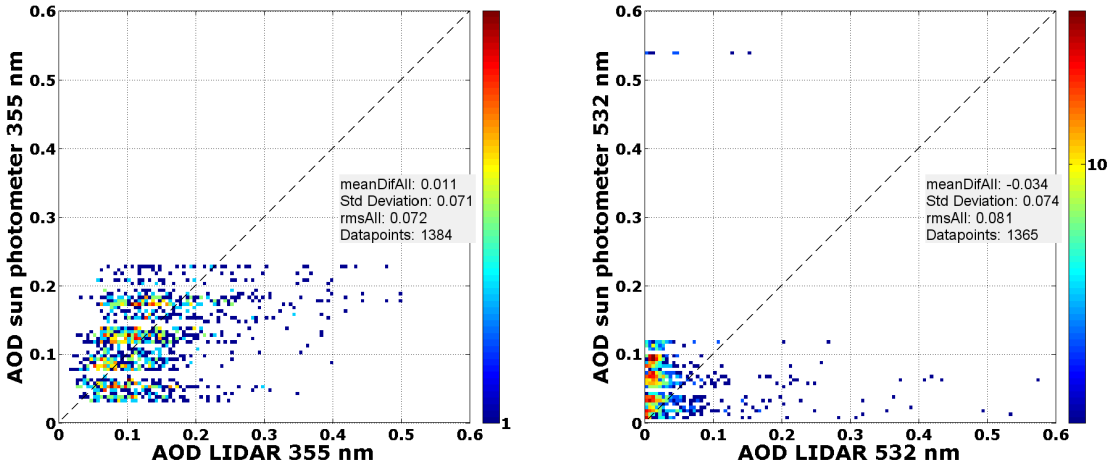

(a) (b)

Figure 27: *AODs of sun photometer and LIDAR for 355 nm (a) and for 532 nm (b) with applied correction function by Guerrero-Rascado et al. (2010) (direct method).*

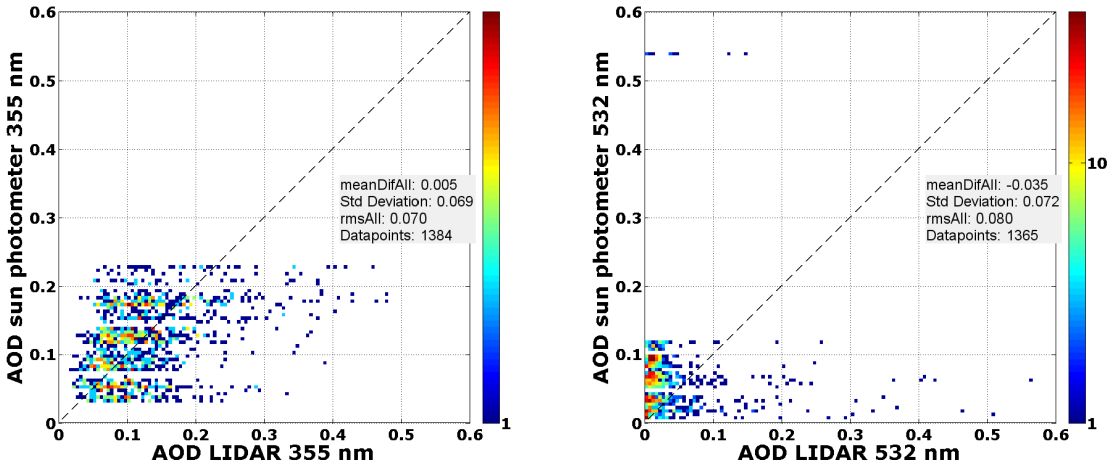

(a) (b)

Figure 28: *AODs of sun photometer and LIDAR for 355 nm (a) and for 532 nm (b) with applied correction function by Guerrero-Rascado et al. (2010) (iterative method).*

For the 335 nm wavelength both correction functions lead to a decreasing number of included data points from 1389 to 1384. The correction function obtained with the *iterative method* leads to smaller errors for the 355 nm wavelengths (MD 0.005, STD 0.069, RMS 0.070) than the usage of the *direct method*. The errors are calculated with the sun photometer AODs as reference values. The correction function obtained with the *direct method* "over-corrects" the signal, as can be seen from the positive value of the mean difference (0.011). Also for the 532 nm wavelength the correction function obtained with the *iterative method* leads to smaller errors, when comparing the AODs of the sun photometer with the AODs of the corrected LIDAR data, see figures 27(a) and 27(b). In that case number of data points is reduced to 1365.

4.3.4 FS11 Comparison

At the PSA also FS11 scattermeter of Vaisala are used to determine the extinction coefficient. As primary measurand, the MOR (Meteorological Optical Range) serves to derive the spectral extinction coefficient using the Beer-Lambert Law. The scattermeter consists of an emitting unit which produces a light beam with a wavelength of 875 nm. The receiver unit measures the monochromatic photons, which are scattered by a small air volume into the receiver optics. One FS11 scattermeter is mounted in a height of about 90 m on the top of the CESA1 tower located at PSA (see figure 29(a) and 29(b).

It is expected that the FS11 extinction coefficient is lower than the extinction coefficient obtained with the LIDAR system, because of the higher wavelength. To reach the region of complete overlap for the LIDAR system already at an altitude of 90 m, the LIDAR was tilted to an elevation angle of 20° and 15° for separate measurements at 2014/06/11 at 12:19-12:48 pm and at 13:21-13:50 pm, respectively.

(a) **(b)**

Figure 29: *(a) Tower and (b) scattermeter at the PSA.*

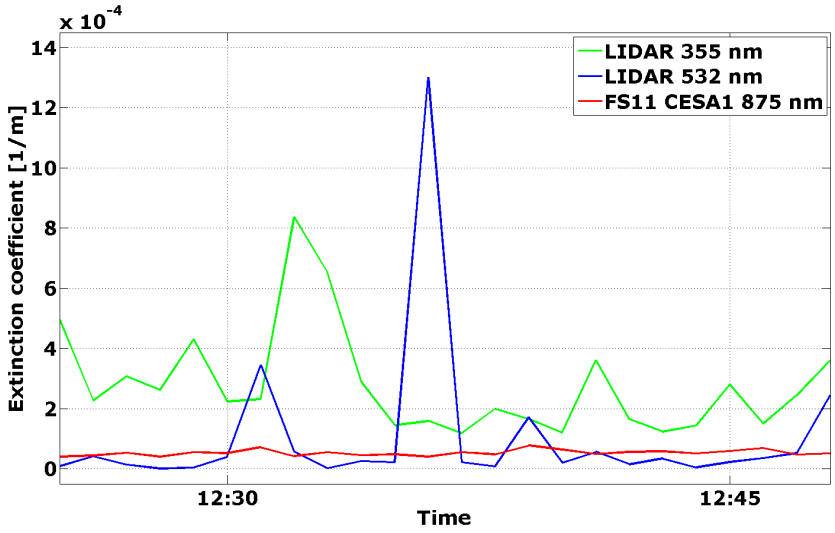

(a)

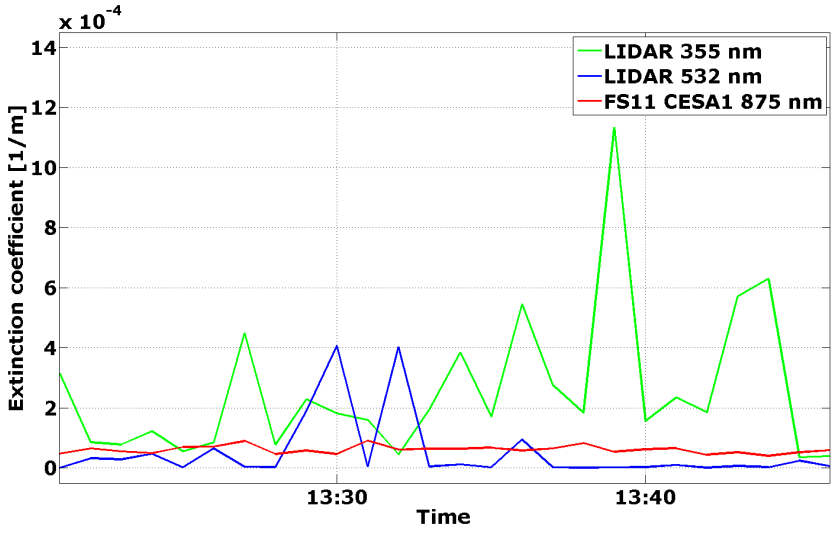

(b)

Figure 30: *Extinction coefficient at 90 m altitude obtained by FS11 CESA1 and LIDAR with 20° elevation (a) and 15° elevation (b). Recorded on 2014/06/11.*

In figure 30, the extinction coefficient $\alpha(r, \lambda)$ measured with the FS11 scattermeter and the LIDAR system is shown. Figure 30(a) shows the extinction coefficient for the LIDAR wavelengths 355 nm and 532 nm for an elevation angle of 20° compared to the extinction coefficient measured with the FS11 for the 875 nm wavelength. The temperature and pressure profiles have been adapted for the calculation of the extinction coefficient. For the 15° measurement, the reference altitude was adapted from 5000 m to the highest possible altitude 3882 m.

As expected, the LIDAR 355 nm extinction coefficient is higher than for the other wavelengths. For the 532 nm wavelength, a large fraction of the determined extinction coefficients are below the values measured with the FS11. This could be due to the range correction that is applied to the LIDAR signal. The backscatter signal is mul-

tiplied with r^2 for the respective sampling altitude to correct the assumed logarithmic decrease in signal for increasing altitudes. For angular measurements this correction may be insufficient, because a smaller amount of the direct solar radiance reaches the receiver.

Furtermore, the LIDAR extinction measurements show higher peaks, due to a higher sensitivity compared to the FS11. A general source of error for the comparison of LIDAR and FS11 is the inhomogeneity of the atmosphere. Although the FS11 and the LIDAR recorded signals at the same altitudes, the distance between the atmospheric sampling points is approximately 1 km. Thus, the extinction coefficient may vary strongly due to fluctuations in aerosol and molecule density.

Figure 30(b) shows the extinction coefficients for the different LIDAR wavelengths recorded with an elevation angle of 15° of the LIDAR system, compared to the extinction coefficient measured with the FS11 for the 875 nm wavelength. Again, the LIDAR wavelengths show a stronger sensitivity, reflected by high peaks, whereas the extinction coefficient measured with the FS11 lies constantly below the range of 10^{-5}. Particularly, extinction coefficient determined from the 532 nm wavelength lies below the FS11 extinction coefficient. A reason for the lower values at this wavelength is the negative range corrected signal at the reference height. The 532 nm lidar signal is more distrubed by noise signals and therefore tends to negative signals at the reference height, resulting in a low or negative extinction coefficient for the corresponding altitude. Nevertheless, figure 30 shows that the calculated extinction coefficients for the LIDAR system are in good accordance with the reference values obtained with the FS11.

To evaluate the correction functions not only by comparing to sun photometer data, the extinction coefficient from the corrected signal of vertical LIDAR measurements can also be compared with the extinction coefficient obtained with the FS11. For that aim, the three correction functions are applied to the lidar signals. Data were recorded on the 2014/03/05 between 11:37 am and 15:38 pm. Figure 31(a) shows the LIDAR extinction coefficient derived from the 355 nm measurement for the correction functions earlier stated in section 2.7 and shown in figure 22. Additionally, the derived extinction coefficients from the uncorrected lidar signal and the FS11 data is shown. The data were obtained for an altitude of 90 m.

In figure 31(a) the lidar extinction coefficients for the 355 nm channel is shown. If no correction is applied, the extinction coefficient is negative as expected for altitudes lower than the complete overlap region beginning at 120 m. The application of the correction function proposed by Stelmaszczyk et al. (2005) results in a negative extinction coefficient. A significant change is obtained with the correction function proposed by Biavati et al. (2011) and the iteratively obtained correction function by Guerrero-Rascado et al. (2010). For the 532 nm LIDAR channel, the analogous measures are illustrated in figure 31(b). Again, the stronger influence of background radiation for higher wavelengths is reflected in the depicted results. At the reference height, noise signals lead to negative values after background correction, resulting in a negative extinction coefficient.

A direct comparison to the FS11 values underlines the need of a correction function for the region of incomplete overlap. According to the previously described results of section 4.3.2 and section 4.3.3, the proposed correction function by Biavati et al. (2011) and the iteratively obtained correction function by Guerrero-Rascado et al. (2010) are

best suited. After correction of the signal the extinction coefficient lies in good accordance to the reference values obtained with the FS11.

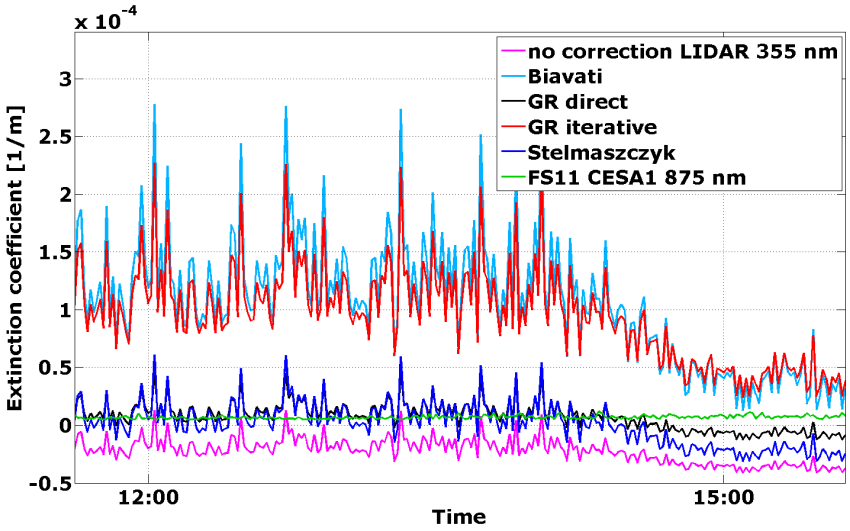

(a)

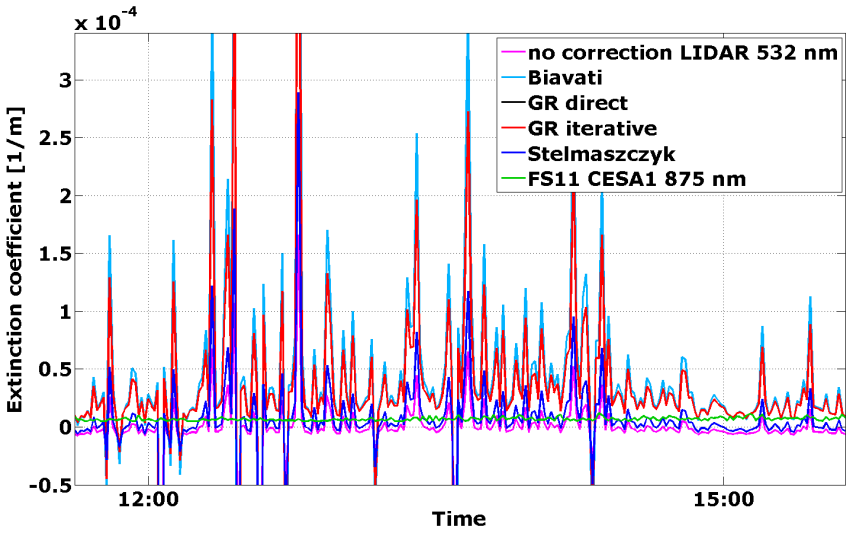

(b)

Figure 31: *Extinction coefficient at 90 m altitude obtained by FS11 CESA1 and LIDAR with applied correction functions for* 355 *nm (a) and* 532 *nm (b). Recorded on 2014/03/05.*

5 Conclusion and Outlook

The determination of the aerosol extinction coefficient by LIDAR measurements and the comparison with results of simultaneously recorded measurements by sun photometer and ceilometer were the main goal of this study. As described in the previous sections, there are multiple factors, dependent of environmental conditions and the measuring set-up, that have significant influence on the results.

For LIDAR analysis, data were acquired between the 2013/08/02 and the 2014/06/20 with a total amount of 33:32 h measurement time. For data processing suited MATLAB routines were developed. The backscatter signals of the 355 nm and 532 nm elastic LIDAR channels were analyzed using the Klett-Fernald method, as it is a stable solution method for determination of the backscatter and extinction coefficients [Klett, 1981]. Pressure and temperature standard profiles were scaled to on-site ground values for application in the calculation of the molecular backscatter and extinction coefficients.

Additionally, assumptions for the reference height and the lidar ratio have been made as required by this method. These assumptions were made on the basis of the performed sensitivity studies regarding the reference height, lidar ratio and background correction and with respect to existing literature. In fact, the reference height was set to 5000 m, and the lidar ratios to 58 sr for the 355 nm wavelength and 55 sr for the 532 nm wavelength. For background correction, the mean backscatter signal from the region between 14 675 m and 15 000 m was subtracted from the overall signal.

The choice of the reference height and the lidar ratio is atmosphere dependent and varies for different measurement sites. As the influence to the derived backscatter and extinction coefficients is large, the determination of both parameters prior to calculations is of equal importance. The choice of background correction parameters, such as the range where no signal is expected, is of secondary importance, as its impact on the calculations is less significant. Nevertheless, the results exhibit that, generally, a background correction for the raw backscatter signal is necessary.

Recorded data of the sun photometer and the ceilometer were compared to the resulting extinction measurements from the LIDAR system. The sun photometer provides values for the AOD by measuring the relative luminescence. The data processing by the Aerosol Robotic Network (AERONET) includes inter alia the level 1.5 retrieval algorithm that excludes all data acquired under cloudy atmospheric conditions. Therefore, the comparison of sun photometer and LIDAR AODs was accomplished with data from ≈ 23 h measurement at exclusively cloud-free time periods between the 2014/03/04 and the 2014/03/20. For the 355 nm wavelength the mean difference between the AODs determined with the sun photometer and the LIDAR of -0.004 was determined. An increase in aerosol extinction in the atmosphere, due to a temporal increase of the number of particles in air, is equally detected by both instruments. With the 532 nm LIDAR channel, lower AODs than for the sun photometer were determined, caused by the incomplete overlap of the laser's and the receiver's fields of view.

Furthermore, a comparison of the ceilometer AODs and the LIDAR AODs was accomplished for data recorded between the 2014/03/03 and the 2014/03/20 involving a total time of measurement of ≈ 24 h. As an advantage, also time periods with cloudy atmospheric conditions could be analyzed, leading to an additional included measurement time of ≈ 10 h compared to the sun photometer. Since the ceilometer is also based on the LIDAR technology, the retrieval of the aerosol extinction coefficient was analogous

for both types of backscatter signals. The lidar ratio was set to 45 sr for the 1064 nm wavelength. The results revealed significantly lower extinction coefficients measured by the ceilometer elastic backscatter channel at a wavelength of 1064 nm than by LIDAR measurements. This deviation was found to increase under hazy or cloudy conditions. A source of error could be a possible misalignment of the ceilometer system. The laser beam could exit the FOV of the receiver below the reference range is reached, so that the backscatter signals are smaller. Nevertheless, a misaligned ceilometer system is an improbable source of error, that could be corrected by a system calibration. Another possible explanation for errors of the ceilometer backscatter signal, is a malfunction of the ceilometer correction function. The output signal is corrected by an implemented correction function by Jenoptik that aims to correct the reduced signal in the region of incomplete overlap of the ceilometer.

A comparison between the ceilometer and the sun photometer was accomplished. The Ångström approach allows to modify the sun photometer AODs of the 1020 nm channel to the specific 1064 nm wavelength of the ceilometer. Thus, the AODs of both instruments can be compared without wavelength dependent deviations in the corresponding AODs. Data correspond to a total time of 738 h of measurement between the 2013/11/07 and 2014/06/24 with cloud-free atmospheric conditions. The AODs of the ceilometer are significantly lower than these of the sun photometer, supporting the assumption of a misalignment of the ceilometer's set up. Another source of error was found in the high signal-to-noise ratio of the ceilometer signal at the reference altitude.

To correct the signal loss below the complete overlap region of the LIDAR system, the correction functions proposed by Stelmaszczyk et al. (2005), Biavati et al. (2011) and Guerrero-Rascado et al. (2010) were analyzed. Therefore, the correction functions were implemented and applied to the lidar backscatter signal. The aerosol extinction coefficient is expected to decrease with altitude for clear atmospheres and hence reaches its maximum at ranges close to the ground.

The correction function proposed by Stelmaszczyk et al. (2005), solely retrieved from geometrical considerations respecting the LIDAR system, has a small impact on the signal in the region below 120 m. Nevertheless, comparing all correction functions regarding deviation to the reference AODs by the sun photometer, it is found to be the best suited correction method for the 355 nm wavelength lidar signal, since the deviations are minimized. On the other hand, it has no impact on the results for the 532 nm LIDAR channel. For that reason this correction function is not suited for the LIDAR system.

A significant impact on the signal and the according aerosol extinction coefficient could be verified for the correction function proposed by Biavati et al. (2011). This correction function is valid for the region above 45 m. Comparison to sun photometer data shows that the 355 nm wavelength signal is "over-corrected" as it leads to higher AODs than the reference AODs of the sun photometer. For the 532 nm wavelength the AODs after signal correction are in good accordance to the reference AODs of the sun photometer.

From the deviation analysis for the 532 nm wavelength can be seen that the correction function proposed by Guerrero-Rascado et al. (2010), determined with the iterative approach suits best for signal correction, because the deviations are minimized. This correction function is retrieved from the ceilometer attenuated backscatter coefficient. The ceilometer backscatter signal is valid for the region above 15 m and thus can

account for the lidar signal correction down to 15 m. This correction function fulfills the expectation that the AODs for both wavelengths are corrected in agreement to the reference AODs. Therefore, the correction function proposed by Guerrero-Rascado et al. (2010), obtained with the iterative method, is the best suited method for the LIDAR system.

Finally, the extinction coefficient acquired with the lidar signals from tilted measurements and a Vaisala FS11 scattermeter was compared. The scattermeter is installed at 90 m altitude. Angular LIDAR measurements have been performed with 20° and 15° elevation. For both measurements a smaller extinction coefficient at the 532 nm wavelength than for the 875 nm scattermeter extinction coefficient was obtained. An explanation is the horizontal inhomogeneity of the atmosphere, since different samples of air are measured. Comparison of the corrected extinction coefficient of the LIDAR to the scattermeter data shows that after correction with the correction function proposed by Guerrero-Rascado et al. (2010) the extinction coefficients lie in good accordance. A deviation of peak intensity is explained by atmospheric inhomogeneity.

To obtain more accurate results of extinction coefficients and consequently of the aerosol optical depth, further investigation of the lidar ratio is necessary [Wiegner and Geiß, 2012]. For this purpose the LIDAR system provided by Raymetrics allows optional extension of the polarized detection channels.

LIDAR systems offer promising possibilities for a more precise understanding of optical and chemical properties of the earth's atmosphere. Especially, extinction profiles with high temporal resolution are of interest for CSP technology. Information about the aerosol distribution in the lower boundary layer is primarily important for solar resource assessment, as concentrating solar tower plants suffer more from atmospheric extinction than for example parabolic through plants. More measurement campaigns with high technology LIDAR systems next to commercially available instruments like the FS11 Vaisala scattermeter will probably allow a better understanding of the working principles and drawbacks of the more simple commercial instruments. That may lead to the possibility of a more accurate resource assessment even with these commercial instruments in the future.

References

[Abdullah et al., 2013] Abdullah, F. T., Lim, K., Welton, E. J., and Lolli, S. (2013). An initial assessment of ground based lidar backscattered signal in penang island. *Proceeding of the 2013 IEEE International Conference on Space Science and Communication, Melaka, Malaysia.*

[Ackermann, 1998] Ackermann, J. (1998). The extinction-to-backscatter ratio of tropospheric aerosol: A numerical study. *Journal of Atmospheric and Oceanic Technology, Vol. 15.*

[AERONET, 2014] AERONET (2014). Aeronet, http://aeronet.gsfc.nasa.gov/. [online, accessed august 2014].

[Anderson et al., 1986] Anderson, G., Clough, S., Kneizys, F., Chetwynd, J. S., and E.P. (1986). Afgl atmospheric constituent profile (0-120km). *Environmental Research, No. 954.*

[Ansmann et al., 1990] Ansmann, A., Riebesell, M., and Weitkamp, C. (1990). Measure of atmospheric aerosol extinction profiles with raman lidar. *Optical Letters, 15, 746-748.*

[Ansmann et al., 1992] Ansmann, A., Riesebell, M., Wandinger, U., Weitkamp, C., and Michaelis, W. (1992). Independent measurement of extinction and backscatter profiles in cirrus clouds by using combined raman elastic-backscatter lidar. *Applied Optics 29.*

[Benito, 2001] Benito, R. V. (2001). Atmospheric aerosol chracterization. *Óptica Pura y Aplicada, Vol. 34.*

[Berkoff et al., 2003] Berkoff, T. A., Welton, E., Campbell, J., Scott, V., and Spinhirne, J. (2003). Investigation of overlap correction techniques for the micro-pulse lidar network (mplnet). *IEEE.*

[Biavati et al., 2011] Biavati, G., Donfrancesco, G. D., Cairo, F., and Feist, D. G. (2011). Correction scheme for close-range lidar returns. *Optical Society of America, Applied Optics, Vol. 50, No.30.*

[Bird and Riordan, 1984] Bird, R. and Riordan, C. (1984). Simple solar spectral model for direct and diffuse irradiance on horizontal and tilted planes at the earth's surface for cloudless atmospheres. *Solar Energy 32, 461-471.*

[Bissonnette et al., 2002] Bissonnette, L., Roy, G., Poultier, L., Cober, S., and Isaac, G. (2002). Multiple-scattering lidar retrieval method: tests on monte carlo simulations and comparisons with *in situ* measurements. *Applied Optics, 41.*

[Cimel, 2001] Cimel (2001). Cimel sun photometer, user manual.

[Curcio and Knestrick, 1958] Curcio, J. A. and Knestrick, G. L. (1958). Correlation of atmospheric transmission with backscattering. *Journal of the Optical Society of America, Vol. 48, Num. 10.*

[Fernald et al., 1972] Fernald, F., Herman, B., and Reagan, J. (1972). Determination of aerosol height distribution by lidar. *J. Appl. Meteorol., 11, 482-489.*

[Freudenthaler, 2008] Freudenthaler, V. (2008). A quality assurance tool for the optical part of a lidar system. *24th International Laser Radar Conference, Boulder.*

[Fröhlich and Shaw, 1980] Fröhlich, C. and Shaw, G. E. (1980). New determination of rayleigh scattering in the terrestrial atmosphere. *Applied Optics, Vol. 19, 11.*

[Goyer and Watson, 1963] Goyer, G. and Watson, R. (1963). The laser and its application to meteorology. *Bulletin of the American Meteorological Society. 44 (9): 564575.*

[Groß, 2011] Groß, M. (2011). *Aerosol characterization by multi-wavelength Raman- and depolarization lidar observations.* PhD thesis, Ludwig-Maximilians-Universität.

[Groß et al., 2011] Groß, S., Tesche, M., Freudenthaler, V., Toledano, C., Wiegner, M., Ansmann, A., Althausen, D., and Seefeldner, M. (2011). Characterization of saharan dust, marine aerosols and mixtures of biomass burning aerosols and dust by means of multi-wavelength depolarization- and raman-measurements during samum-2. *Tellus, B, 63: 706-724.*

[Guerrero-Rascado et al., 2010] Guerrero-Rascado, J. L., João Costa, M., Bortoli, D., Silvia, A. M., and Lyamani, H. Alados-Arboledas, L. (2010). Infrared lidar overlap function: an experimental determination. *Optical Society of America, Optics Express.*

[Guerrero-Rascado et al., 2008] Guerrero-Rascado, J. L., Ruiz, B., and Alados-Arboledas, L. (2008). Multi-spectral lidar characterization of the vertical structure of saharan dust aerosol over southern spain. *Atmospheric Environment, 40, 2668-2681.*

[Gueymard, 2001] Gueymard, C. (2001). Parameterized transmittance model for direct beam and circumsolar spectral irradiance. *Solar Energy 71,No.5,325-346.*

[Gutkowicz-Krusin, 1993] Gutkowicz-Krusin, D. (1993). Multiangle lidar performance in the presence of horizontal inhomogeneities in atmospheric extinction and scattering. *Applied Optics, 32, 3266-3272.*

[Hanrieder et al., 2012] Hanrieder, N., Wehringer, F., W. S., Wolferststetter, F., Pitz-Paal, R., A., C., and Quaschning, V. (2012). Determination of beam attenuation in tower plants. *SolarPACES, Marrakech, Marokko.*

[Holben et al., 1998] Holben, B., Eck, T., I., S., Tanré, D., Buis, J., Setzer, A., Vermote, E., Reagan, J., Kaufman, Y., Nakajima, T., Lavenu, F., Jankowiak, I., and Smirnov, A. (1998). Aeronet - a federated instrument network and data archive for aerosol characterization. *Remote Sensing of Evironment, Vol. 66, 1-16.*

[Ince, 1956] Ince, E. (1956). *Ordinary Differential Equations.* Dover, New York.

[Jenoptik, 2013] Jenoptik (2013). Chm 15k - nimbus ceilometer, user manual.

[King, 1923] King, L. V. (1923). On the complex anisotropic molecule in relation to the dispersion and scattering of light. *Proc. R. Soc London, Ser. A, 104, 333-357.*

[Kittel, 1976] Kittel, C. (1976). *Introduction to Solid State Physics.* 5th ed., Chap. 2, Wiley, New York, USA.

[Klett, 1981] Klett, J. D. (1981). Stable analytical inversion solution for processing lidar returns. *Applied Optics, 20, 211-220.*

[Kovalev, 2004] Kovalev, V. A. & Eichinger, W. E. (2004). *Elastic Lidar: Theory, Practice, and Analysis Methods.* Wiley, New York, USA.

[Kunz and de Leeuw, 1993] Kunz, G. J. and de Leeuw, G. (1993). Inversion of lidar signals with the slope method. *Applied Optics, 32, 3249-3256.*

[Kuze et al., 1998] Kuze, H., Kinjo, H., Sakurada, Y., and Takeuchi, N. (1998). Field-of-view dependence of lidar signals by use of newtonian and cassegrainian telescopes. *Applied Optics , 37, 3128-3132.*

[Lange et al., 2011] Lange, D., Kumar, D., Rocadenbosch, F., Sicard, M., and Comerón, A. (2011). Optimized data-gluing method for mixed analog/photon counting lidar signals. *Revista Boliviana de Física 20s, 4-6.*

[Licel, 0011] Licel (20011). Licel ethernet controller - installation and reference manual.

[Mattis et al., 2008] Mattis, I., Müller, D., Ansmann, A., Wandinger, U., Preißler, J., Seifert, P., and Tesche, M. (2008). Ten years of multiwavelength raman lidar observations of free-tropospheric aerosol layers over central europe: Geometrical properties and annual cycle. *Journal of Geophysical Research, Vol. 113, D20202.*

[Mielke, 2005] Mielke, B. (2005). Analog + photon counting, http://www.licel.com/analogpc.pdf/. [online, accessed august 2014]. *Licel Tech. Note, 10 pp.*

[Mona et al., 2007] Mona, L., Amodeo, A., D'Amico, G., and Pappalardo, G. (2007). First comparisons between cnr-imaa multiwavelength raman lidar measurements and calipso measurements. *Proc. SPIE 6750.*

[Müller et al., 2007] Müller, D., Ansmann, A., Mattis, I., Tesche, M., Wandinger, U., Althausen, D., and Pisani, G. (2007). Aerosol-type-dependent lidar ratios observed with raman lidar. *Journal of Geophysical Research, Vol. 112, D16202.*

[Parsiani and Bonilla, 2008] Parsiani, H. and Bonilla, A. (2008). Aerosol size distribution estimation using sun photometer and artificial neural network. In *12th WSEAS International Conference on SYSTEMS, Heraklion, Greece.*

[Pitman and Vant-Hull, 1982] Pitman, C. and Vant-Hull, L. (1982). Atmospheric transmission model for a solar beam propagating between a heliostat and receiver. *Proc. Annu. Meet.-Am. Sect. Int. Sol. Energy Soc., Houston, USA.*

[Quaschning, 2012] Quaschning, V. (2012). *Regenerative Energiesysteme, Technologie - Berechnung - Simulation.* Hanser.

[Raymetrics, 2012] Raymetrics (2012). Lr201-vu-d300 lidar system, technical specifications.

[Sasano et al., 1985] Sasano, Y., Browell, E., and S., I. (1985). Error caused by using a constant extinction/backscattering ratio in the lidar solution. *Applied Optics, Vol.24, No.22.*

[Shipley et al., 1983] Shipley, S. T., Tracy, D. H., Eloranta, E. W., Trauger, J. T., Stroga, J. T., Roesler, F. L., and Weinman, J. A. (1983). High spectral resolution lidar to measure optical scattering properties of atmospheric aerosols. 1.theory and instrumentation. *Applied Optics, 22, 3716-3724.*

[Smirnov et al., 2000] Smirnov, A., Holben, B., Eck, T., Dubovik, O., and Slutsker, I. (2000). Characterization quality control algorithms for the aeronet database. *Remote Sensing Environment, Vol. 73, 337-349.*

[Sneep and Ubachs, 2005] Sneep, M. and Ubachs, W. (2005). Direct measurement of the rayleigh scattering cross section in various gases. *Journal of Quantitative Spectroscopy Radiative Transfer 92.*

[Stelmaszczyk et al., 2005] Stelmaszczyk, K., Dell'Aglio, M., Chudzyński, S., Stacewicz, T., and Wöste, L. (2005). Analytical function for lidar geometrical compression form-factor calculations. *Optical Society of America, Applied Optics, Vol. 44, No. 7.*

[Stoyanov et al., 2012] Stoyanov, D., Grigorov, I., Kolarov, G., Peshev, Z., and Dreischuh, T. (2012). *Advanced Photonic Sciences.* InTech.

[Takamuka et al., 1994] Takamuka, T., Reagan, J. D., and Herman, B. M. (1994). Tropospheric aerosol optical properties derived from lidar, sun photometer and optical counter measurements. *Applied Optics, 33, 7132-7140.*

[Waggoner et al., 1972] Waggoner, A. P., Ahlquist, N. C., and Charlston, R. J. (1972). Measurement of the aerosol total backscatter ratio. *Applied Optics, 11, 2886-2889.*

[Wandinger and Ansmann, 2002] Wandinger, U. and Ansmann, A. (2002). Experimental determination of the lidar overlap profile with raman lidar. *Optical Society of America.*

[Wiegner et al., 2012] Wiegner, M., Gasteiger, J., Groß, S., F., S., Freudenthaler, V., and Forkel, R. (2012). Characterization of the eyjafjallajkull ash-plume: Potential of lidar remote sensing. *J Phys. Chem. Earth, 45-46, p 79-86.*

[Wiegner and Geiß, 2012] Wiegner, M. and Geiß, A. (2012). Aerosol profiling with the jenoptik ceilometer chm15kx. *Atmos. Meas. Tech., 5, 1953-1964.*

[Zdunkowski et al., 2007] Zdunkowski, W., Trautmann, T., and Bott, A. (2007). *Radiation in the Atmosphere, A Course in Theoretical Meteorologie.* Cambridge University Press.

List of Figures

List of Tables

Danksagung

Allen voran danke ich Herrn Prof. Dr. Bernhard Mayer für die Möglichkeit, meine Masterarbeit am Meteorologischen Institut der Universität München schreiben zu dürfen.

Dann möchte ich mich ganz besonders bei Frau Natalie Hanrieder für ihre konstruktive, tiefgehende und kontinuierliche Betreuung bedanken. Durch ihr Engagement bot sich mir die Chance, meine Masterarbeit beim DLR in Almeria schreiben zu können und während meines Aufenthaltes stand mir ihre Tür stets offen und sie selbst darüber hinaus für Rat, Ideen und einen wissenschaftlichen Gedankenaustausch zur Verfügung.

Weiterer Dank gilt auch den Kollegen und Studenten des DLR in Almería. Speziell möchte ich mich bei Herrn Dr. Marc Röger für die fachlichen Gespräche und die Tips rund ums Arbeitsleben bedanken. Außerdem danke ich Herrn Christoph Prahl für die motivierenden Worte und die MATLAB Hilfe, Herrn David Schüler für die geistreichen Pausenspäße auf dem Dach und Herrn Sebastian Müller für die gelungene Arbeitsplatzatmosphäre.

Besonders herzlich möchte ich mich auch bei meiner Family bedanken, die mir stets die Kraft gibt, meine Vorhaben umzusetzen und mir entfernungsunabhängig immer zur Seite steht. Danke für die Besuche und die kleinen "sobrinos".

Zuletzt bin ich meinen Eltern und dem Stipendienprogramm PROSA$^{\text{LMU}}$ für die finanzielle Unterstützung zu Dank verpflichtet.

Meinen Aufenthalt in Almería habe ich als sehr spannende, interessante und lehrreiche Zeit wahrgenommen, die meinen Erfahrungsschatz bereichert und mir viel Freude bereitet hat.

Erklärung

Hiermit erkläre ich, die vorliegende Arbeit selbständig verfasst zu haben und keine anderen als die in der Arbeit angegebenen Quellen und Hilfsmittel benutzt zu haben.

Berlin, 12.12.2014

Juliane Ludwig